Design and Implementation of a Controller for an Electrostatic MEMS Actuator and Sensor

by

Abdulrahman Seleim

A thesis
presented to the University of Waterloo
in fulfillment of the
thesis requirement for the degree of
Master of Applied Science
in
Systems Design Engineering

Waterloo, Ontario, Canada, 2010

I hereby declare that I am the sole author of this thesis. This is a true copy of the thesis, including any required final revisions, as accepted by my examiners.

I understand that my thesis may be made electronically available to the public.

Abstract

An analog controller has been analyzed and built for an electrostatic micro-cantilever beam. The closed loop MEMS device can be used as both actuator and sensor. As an actuator it will have the advantage of large stable travel range up to 90% of the gap. As a sensor the beam is to be driven into chaotic motion which is very sensitive changes in the system parameters.

Two versions of the controller have been analyzed and implemented, one for the actuator and one for the sensor. For the actuator, preliminary experiments show good matching with the model. As for the sensor, the dynamic behavior have been studied and the best operating regions have been determined.

Acknowledgements

I would like to express my gratitude to my supervisors Dr. Eihab Abdel-Rahman and Dr. Glenn Heppler. They provided me with guidance, support, and motivation and dedicated a lot of their busy schedule to train me during the last two years. Either directly or indirectly, they taught me a lot in research, technical writing, problem solving, and team work. I would like to add special thanks to Dr. Eihab for spending many evenings with me revising this thesis. In brief, I enjoyed working with them and I wish all supervisors are as wonderful as them.

Words would not be enough to thank my wife. She provided me with endless love and support during the last two years.

Special thanks to my father and mother who brought me to this life and provided me with love and guidance.

I would also like to thank my friends who made the last two years full of fun. Special thanks to Mahmoud Khater, my office mate, and Ahmed Bayoumy for helping me in the electronic circuits design and sharing wonderful evenings together.

All thanks to my Lord, who created me, provided me with everything, and made all this possible.

Dedication

To my mother, father, and wife.

Contents

List of Tables

List of Figures

Chapter 1

Introduction

1.1 Motivation

The MEMS industry grew quickly over the past two decades from a rich research area into a multi-billion dollar industry. Very broadly, MEMS devices are usually classified into two categories namely sensors and actuators. MEMS actuators are used commercially in many applications including, inkjet heads [3, 4, 5, 6], micro pumps [7], RF switches [8, 9], micro-mirror manipulators [10, 11, 12], robotic surgery [13], micro-grippers [14, 15, 16, 17, 18, 19], and probe-based disc drives [20]. In addition to having small size, MEMS actuators have the advantage of low cost, ease of integration with electronic components on one chip and high precision.

MEMS are divided into four groups based on the method of actuation. These groups are electrostatic, thermal, piezoelectric, and electromagnetic. Electrostatic actuation has the advantages of [21, 22]:

- High speed as compared to thermal actuation.

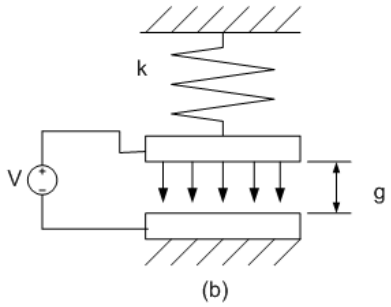

Figure 1.1: Concept of electrostatic actuation.

- Ease of fabrication and integration with CMOS technology, as compared to piezoelectric actuation that requires deposition of ceramic materials which is both challenging and expensive.

- High energy density as compared to electromagnetic actuation.

In electrostatic actuation, two electrodes are set to move relative to each other, Figure 1.1, under the influence of an electrostatic force that arises due to a voltage difference between the electrodes. The electrostatic force is directly proportional to square the voltage difference between the electrodes and inversely proportional to the gap between them.

In MEMS, electrostatic actuation is realized by cantilever beams, fixed-fixed beams, or comb-drives, Figure 1.2. In all cases, the electrostatic force pulls against an elastic restoring force, and the position of the actuator is determined by the balance between the two forces [23].

The major drawback of electrostatic actuation is pull-in instability, which takes place when the elastic force is not able any more to balance the growing nonlinear electrostatic force, forcing the moving electrode to suddenly snap into the fixed one. In cantilever beams, pull-in instability limits the travel range of the tip of the beam to less than one third of the gap for static operation [23], and prevents operation in a large range of frequencies

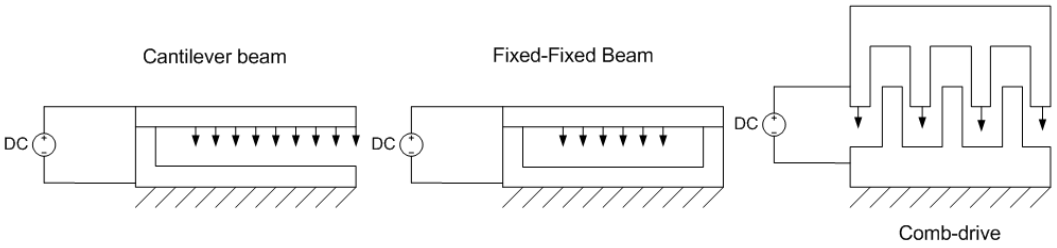

Figure 1.2: Electrostatic actuation types.

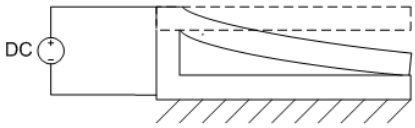

Figure 1.3: Pull-in instability in a micro-cantilever beam.

for dynamic operation [24]. Figure 1.3 shows a micro-cantilever beam after experiencing pull-in.

MEMS electrostatic beams are also used as sensors due to their small size and high sensitivity. Recent applications are mass sensing [25, 26, 27] and mass spectrometry [28]. Sensing is achieved by either measuring the static position change [25] or tracking a change in dynamic behavior as a result of change in the mass of the beam. The change in dynamic behavior can be either a shift in the natural frequency [29, 30] or a sudden change in position (due to a bifurcation) [26, 31].

1.2 Relevant Literature Review

Several approaches have been explored in order to overcome the limited travel range of electrostatically actuated micro-beams. These approaches may be divided into four categories, namely changing the geometric design, adding a series capacitor, charge control,

and feedback control.

Examples of the first category are leveraged bending [22] and curved beams [32]. In leveraged bending, a short electrode is placed under a long beam, the part of the beam above the electrode operates in the stable region while the rest of the beam acts as a lever and moves through larger ranges. The drawback of this approach is the need to use a higher actuation voltage or a bigger device area. In curved beams, the beam is attracted towards a curved electrode. In experiment, it was found that the beam experiences local instabilities and can only be used as a bi-stable structure.

In the second category [33, 34], a series capacitor is added between the beam and the actuation voltage. As the moving beam itself acts as a variable capacitor, the whole system resembles a voltage divider circuit. When the beam moves closer to the electrode, its capacitance increases, thus the voltage across it decreases. Adding the series capacitor resembles the effect of increasing the gap and moving in the stable region of the new gap (which can be equal to the original gap). The drawback of this method is that it requires higher actuation voltages and there is a need to minimize parasitic capacitance in the design.

In the third category, the charge on the electrode is directly controlled using an external circuit [35, 36]. If the electrostatic force is modeled using the charge instead of voltage, the instability disappears and the beam can be positioned anywhere within the gap. This technique uses slightly higher voltage than the open-loop operation, but it requires additional charge control circuitry and leakage current in the order of pico-Ampere should be controlled.

Feedback control was first suggested by Chu and Pister [37]. They used a nonlinear controller in which the input voltage is scaled by the gap. They were able, in simulation, to produce a travel range larger than 80% of the gap. Lu and Fedder implemented position feedback using analog electronics and a capacitor as a position sensor. They used a linear

time-invariant controller to simplify implementation and linearized the system while using gain and phase margin to ensure stability. They were able to obtain a stable travel range of only 60% of the gap [38].

Rocha et al. [39] achieved over 90% of stable travel in experiment using on-off control with capacitive position sensing. A comparator is set to compare the position of the beam with a set position, as long as the position of the beam is lower than the set position, the input voltage is higher than the pull-in voltage. When the beam position is larger than the set position, the input voltage switches to a voltage lower than the pull-in voltage. The beam keeps oscillating around the required position and the ripples magnitude depend on the delays in the controller circuit. The ripples magnitude can be very high and cause pull-in in systems with high Q factor.

Closed-loop control has more advantages over the other methods. It can stabilize the system beyond the pull-in instability in addition to adding robustness to the system against parameter uncertainties and deterioration over time.

Using the same feedback control proposed by Lu and Fedder, Liu et al. [40] observed bi-stability, period doubling bifurcations, and chaotic behavior in an electrostatically actuated micro-cantilever beam. This observation is also reported in a study of the system dynamics by Towfighian et al. [41], targeting mass sensors.

Chaos is the appearance of long-term aperiodic behavior in a deterministic dynamic system that exhibits sensitive dependence on initial conditions. It was first observed in the 1880's by Henri Poincaré; however, useful applications of this interesting phenomenon did not emerge until the 1990's [42]. Chaotic attractors' metrics are highly sensitive to system parameter variations [43]. That is why it can be used in system and parameter identification. Ghafari et al. [44] used the Lyapunov exponent of the chaotic oscillations of rolling elements to detect faults. Yin and Epureanu [45] were able to detect experimentally small variations in the mass of a cantilever beam by detecting changes in the attractor

shape after driving it chaotically. Epureanu el al. [46] were able to detect damage in thermo-shielding panels undergoing chaotic oscillations. Wu et al. [47] used the 3D fractal dimension of the fetal cortical surface to assess the maturation of cortical development and to detect morphologic abnormalities in fetuses.

Chaos in MEMS was observed by Bienstman et al. [48] when using an electrostatically actuated impact resonator, Wang et al. [49], and DeMartini et al. [50]. Bienstamn et al. [48] used a simple fixed-fixed beam driven by a voltage larger than the pull-in voltage. When the beam pulls in, a short circuit is introduced. As a result the voltage drops and the mechanical stiffness becomes larger than the electrostatic force, thus forcing the beam away from the electrode. When the contact is lost, the electric force starts building up again and the beam pulls in again. This switching like operation produces large periodic motions. Chaos was observed in the system and thus tracked to be avoided. Wang et al. [49] used non-overlapping comb-drives thus creating a bi-stable structure similar to the duffing oscillator. They successfully measured chaotic oscillations experimentally. However, there were large mismatches between the model and experiment. The mismatch was mainly due to inability to estimate the system parameters. DeMartini et al. [50] used a similar structure and were also able to produce chaotic motions experimentally.

De and Aluru [51] reported chaos in an open-loop electrostatically actuated parallel-plate resonator prior to pull-in. Najar et al. [52] reported an incomplete cascade of period-doubling bifurcations just before pull-in in electrostatic actuators. They concluded that chaos cannot occur in open-loop electrostatic actuators due to occurrence of homoclinic bifurcation which leads to rapid dynamic pull-in.

1.3 Scope of This Work

In this work, the feedback control strategy developed by Lu and Fedder is utilized to develop a low-frequency actuator with a large stable travel range and a chaotic resonator. The chaotic resonator developed here will be used as a platform to design a mass sensor. The controller is designed and implemented using analog electronics. A vibrometer is used as a sensor in the experiments to close the loop.

The design and implementation of the controller are presented in Chapter 2. Chapter 3 presents the system analysis and realization for using the device as an actuator in addition to experimental results for the closed-loop system. Close-loop experiments were conducted in conjunction with Ms. Towfighian. In Chapter 4 the dynamic analysis of the system is presented for a mass sensor. Conclusions and future work are then presented in Chapter 5.

Chapter 2

Controller Design

2.1 Introduction

Open-loop electrostatically actuated micro-cantilever beams, Figure 2.1(a), can be represented, using lumped-mass modeling, as an equivalent single degree of freedom spring-mass system. In this model, Figure 2.1(b), the effective mass of the beam is approximated as a point mass positioned at the tip of the beam, the distributed electrostatic force is lumped to a single force F acting on the point mass, and the mechanical stiffness of the beam k is lumped to a single spring. Using Euler-Bernoulli beam theory, the spring constant can be approximated as

$$k = \frac{3EI}{L^3} \tag{2.1}$$

where E is Young's modulus, I is the second moment of area, and L is the beam length.

Using Newton's second law, the equation of motion of the lumped-mass can be written

$$m\ddot{d} = -kd + F \tag{2.2}$$

where m is the mass of the beam and $d(t)$ is the displacement of the beam tip in the z

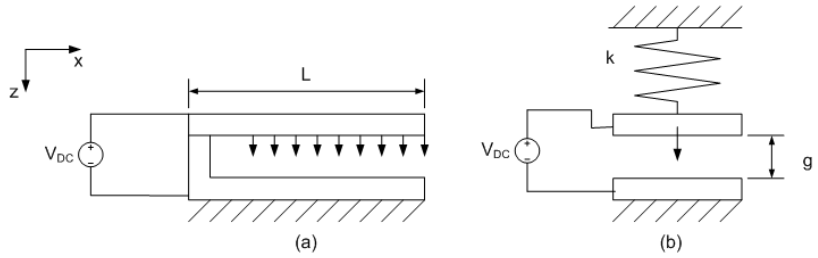

Figure 2.1: Diagram of the cantilever beam.

direction. The electrostatic force F is represented in closed-form by

$$F = \frac{cV_{DC}^2}{(g-d)^2} \tag{2.3}$$

where c is the electromechanical coupling coefficient, V_{DC} is the voltage difference between the two electrodes, and g is the capacitor gap [23]. Equation (2.3) can be presented in first-order form as:

$$\dot{d} = v \tag{2.4}$$

$$\dot{v} = -\frac{k}{m}d + \frac{cV_{DC}^2}{m(g-d)^2} \tag{2.5}$$

where $v(t)$ is the velocity of the beam tip.

For static analysis, $\dot{d}$ and $\dot{v}$ are zero, yielding the two equations:

$$0 = v \tag{2.6}$$

$$0 = -kd + \frac{cV_{DC}{}^2}{(g-d)^2} \tag{2.7}$$

We can rearrange equation (2.7) to obtain

$$d^3 - 2gd^2 + g^2d = \frac{cV_{DC}{}^2}{k} \tag{2.8}$$

The algebraic solutions of equation (2.8) include the equilibrium positions of the beam. Since equation (2.8) is a third-order polynomial, the system has three solutions at every

Table 2.1: Micro-actuator dimensions.

L	200μm
w	80μm
h	4.5μm
g	2μ m

input voltage. Figure 2.2 shows the solutions of the equilibrium equation (2.8) for one of the micro-actuators under study in this work. The actuator dimensions are listed in table 2.1, where L is the beam length, w is the beam width, and h is the beam thickness.

At $V_{DC} = 168$V, two of the solution branches in Figure 2.2 meet in a saddle-node bifurcation and disappear. After this bifurcation two of the roots of equation (2.8) become imaginary. The third root (dash-dotted), is always larger than $2\mu m$. This means that it is aphysical as the beam displacement can not exceed the gap length g.

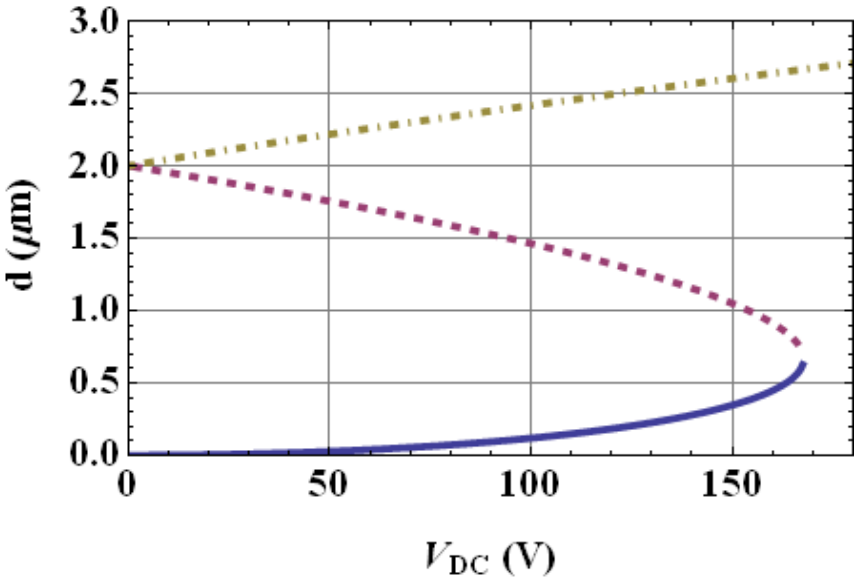

Figure 2.2: Solutions of Equation [2.8] as functions of V_{DC}.

The stability of the equilibrium points can be determined by examining the eigenval-

ues of the Jacobian of the right-hand side of equations (2.6) and (2.7) evaluated at the equilibrium point. The Jacobian of the system is given by

$$J = \begin{bmatrix} 0 & 1 \\ -\frac{k}{m} + \frac{2cV_{DC}{}^2}{m(g-d)^3} & 0 \end{bmatrix}$$

When all the eigenvalues of J have negative real parts, the equilibrium position is said to be asymptotically stable. Otherwise it is unstable. It was found that the solid line in Figure 2.2 is the locus for stable positions and the dashed line is the locus for unstable positions. Beyond the saddle-node bifurcation point, no physical equilibria exist and the moving beam snaps into the fixed electrode in what is called pull-in.

For any stable equilibrium position, the location of the saddle (unstable equilibrium) serves as an upper bound on the maximum realizable oscillations. The range of realizable static positions is limited by the displacement at pull-in.

It is clear from Figure 2.2 that the beam cannot be positioned beyond one-third of the gap length. The control strategy proposed here will seek to stabilize electrostatic micro-actuators beyond their open-loop pull-in voltage by introducing a control voltage that seeks to prevent electrostatic forces from growing in an unbounded fashion as the capacitor gap decreases.

2.2 Close-Loop System

Figure 2.3 shows a block diagram of the system under close-loop control. A commanded voltage signal V_a is inserted to actuate the beam. A vibrometer is used to measure the beam motions and output a voltage signal proportional to the velocity of the beam tip v. This signal is then used to produce a feedback control voltage V_s that is subtracted from the actuation voltage, then the output of the adder is multiplied by a gain G and fed to the beam.

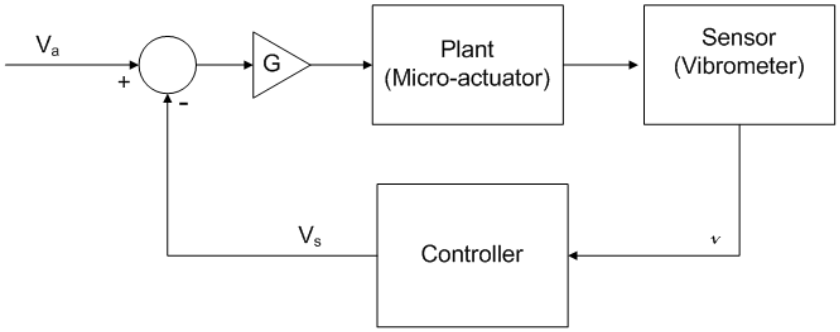

Figure 2.3: The block diagram of the close-loop system.

2.2.1 Plant

The plant under control is an electrostatic actuator composed of a fixed electrode, above which lies a micro-cantilever beam. Figure 2.4 shows a picture of the micro-actuator taken using an optical profilometer. The beam is fabricated using the MUMPs fabrication process. The beam is made of the first structural polysilicon layer Poly 1, the gap is made of the First Oxide sacrificial layer and the electrode is made of the ground polysilicon layer Poly 0.

2.2.2 Controller

The controller realized by Lu et al. [38] uses analog electronics and a capacitor to sense the position of the beam. In this work, a vibrometer is used as a sensor to measure the velocity of the beam tip. Digital and analog control approaches were considered as candidates to realize the control law. Digital control converts the analog signal of the vibrometer into a digital signal and uses a computer to implement the control law. The output digital signal is then converted back to its analog equivalent to close the loop on the micro-actuator. To

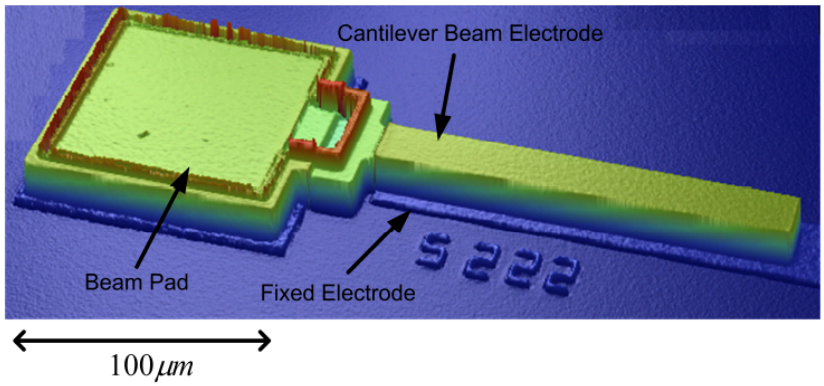

Figure 2.4: A beam-based micro-actuator [1].

implement this control setup one can either use a computer along with a data acquisition card or a microcontroller. As for analog control, an electronic circuit alone fulfills the control law requirements.

The advantages of digital control are simplicity and versatility in both implementing and modifying the control law. All that is needed to implement a new control law or change an existing law is to change a code. On the other hand, it has the disadvantages of high cost, time delays particularly in the analog to digital conversion, and errors due to quantization and discretization. Of course the time delays can be decreased at the cost of using more expensive equipment. As for the analog control, it has the advantages of low cost, minimal time delay, and simple integration of the MEMS plant with the driving electronics. The main disadvantage of analog control is that both the initial design and subsequent modifications of the control law are non-trivial tasks.

The time delays incurred in closing the loop should be negligible compared to the period of free oscillations of the plant $T = 2\pi/\omega$ otherwise they can drive the system to instability [53]. The natural frequency of a cantilever beam is the square root of the ratio of the stiffness to mass. The mass of a cantilever beam scales like the length cubed L^3, while stiffness scales like length L. Dimensional analysis of the natural frequency shows that it

is inversely proportional to the dimensions of the beam

$$\omega = \sqrt{\frac{k}{m}} \propto \sqrt{\frac{L}{L^3}} = \frac{1}{L} \tag{2.9}$$

The dimensions of MEMS actuators are in micro-meters, thus they are typically high-frequency devices. The natural frequencies of the class of micro-beams used in this study range from 65 to 150 kHz. Therefore the minimum period of the plant is $T_{min} = 6.67\mu$s. To meet this requirement, we need to use a ADC with a sampling frequency more than 300kS/s and a time delay less than 0.5μs.

In order to reduce the requirements on the minimum time delay of the controller components, it was decided to use analog control to implement the control law. Further, an electronic bread-board is used to facilitate tuning and modifying the controller parameters in the design and test stages.

2.2.3 Sensor

The vibrometer used, is a Polytech msv 400 which uses the principle of laser interferometry to measure mechanical vibrations. As shown in Figure 2.5, the vibrometer targets a helium-neon laser beam at a point on the surface of a moving object and collects the scattered beam. The optical signal (typically at 40 MHz) is fed into a high frequency signal conditioner. The vibrometer is equipped with decoders to recover the velocity or displacement of a moving point from the optical signal. The velocity of vibration is measured from the frequency difference between the original and the scattered laser beam which arises due to the Doppler effect. The displacement is measured using the phase shift between the two laser beams [2].

The msv 400 used is equipped with the velocity decoder VD-02. The VD-02 can work at frequencies up to 1.5 MHz and outputs an analog signal that represents velocity of the

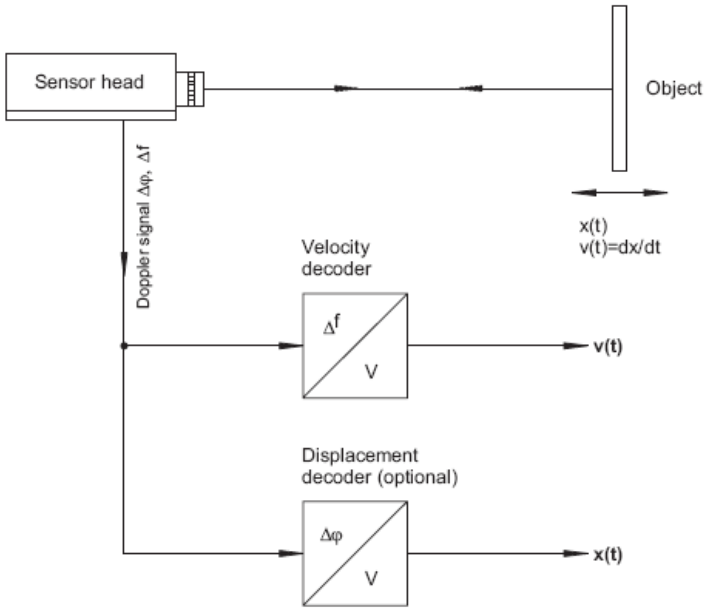

Figure 2.5: Operating principle of the vibrometer [2].

object [54]. The decoder provides the signal scaled to one of four dynamic ranges, namely (5,25,125,1000) mm/s/V with a range of 20 V peak-peak. The dynamic range is set to the smallest admissible acquisition setting so as to obtain the highest possible resolution. The analog signal from the vibrometer is integrated then normalized so that 1 volt is equivalent to a displacement equal to the capacitor gap g. The reason for this normalization is given in the next section.

The normalization is performed as follows. Using the dynamic range of 5mm/s/V means that after integration, 1 volt will represent a displacement of 5mm. Since in the control law, 1 volt should represent a displacement equal to the gap, namely $2\mu m$ therefore, the integrated signal should be multiplied by a gain of $\frac{5\times10^3}{2} = 2500$. If the dynamic range of 25mm/s/V is used, then the gain after the integrator should be equal to $\frac{25\times10^3}{2} = 12500$.

2.3 Control Law Dimensionalization and Realization

After adding the controller, the close-loop system equations, represented in first-order form, are [41]:

$$\dot{d} = v \tag{2.10}$$

$$\dot{v} = -\mu v + \frac{-c_3 d - c_4 d^2 - c_5 d^3 + c_6 G^2 (V_a \sqrt{\alpha} - V_s)^2}{c_0 + c_1 d + d^2} \tag{2.11}$$

$$\dot{V_s} = -r(V_s - \frac{d}{1-d}\Psi\sqrt{\alpha}) \tag{2.12}$$

where $d(t)$ and $v(t)$ represent the displacement and velocity of the tip of the beam in the z direction (Figure 2.1), $V_s(t)$ is the control voltage, $V_a(t) = V_{DC} + V_{AC}\sin(\omega t)$ is the actuation voltage, c_i are non-dimensional modal coefficients obtained from a one-mode Galerkin expansion, μ is the non-dimensional damping coefficient, r is the controller damping, G is the voltage gain, Ψ is the displacement gain and α is the electromechanical coupling coefficient. The tip position, voltage, and time are nondimensionalized with respect to the capacitor gap g, the electromechanical coupling coefficient α, and the time constant of the beam $T = \sqrt{\frac{\rho A L^4}{EI}}$ respectively, where α has the dimensions of $volts^{-2}$, $A = hw$, E is Young's modulus, $I = \frac{wh^3}{12}$ and (L, h, w) are the beam dimensions. The previous equations are derived using a reduced order model for the micro-beam assuming one mode shape. The first two equations govern the position and velocity of the tip of the beam, and the third governs the controller voltage.

The previous equations are represented in a non-dimensional form to improve the stability of numerical simulations. In order to realize the controller, we re-dimensionalize the controller equation by using the dimensional variables $\hat{V_s}$ and $\hat{t}$, where $\hat{V_s} = \frac{V_s}{\sqrt{\alpha}}$ and $\hat{t} = tT$. As a result, the dimensional control voltage $\hat{\dot{V}_s}$ becomes

$$\hat{\dot{V}_s} = \frac{d\hat{V_s}}{d\hat{t}} = \frac{1}{T\sqrt{\alpha}}\frac{dV_s}{dt} \tag{2.13}$$

substituting for $\frac{dV_s}{dt}$ from (2.12) gives:

$$\hat{\dot{V}}_s = \frac{1}{T\sqrt{\alpha}}[-r(\hat{V}_s\sqrt{\alpha} - \frac{d}{1-d}\Psi\sqrt{\alpha})] = \frac{-r}{T}(\hat{V}_s - \frac{d}{1-d}\Psi) \tag{2.14}$$

Note that there is no need to dimensionalize d since it appears in a ratio form. However, when implementing the controller, the voltage representing d should be scaled so that a travel equal to the capacitor gap is equal to 1 Volt. Otherwise, the ratio $\frac{d}{1-d}$ would have to be redimensionalized.

Figure 2.6 shows a block diagram for the control law. A voltage signal representing the displacement is subtracted from a 1 volt input voltage. Then the displacement signal is divided by the output. In the next stage, the signal is multiplied by the displacement gain Ψ. In the final stage, a unit feedback loop exists with a forward path containing a gain $\frac{r}{T}$ and an integrator.

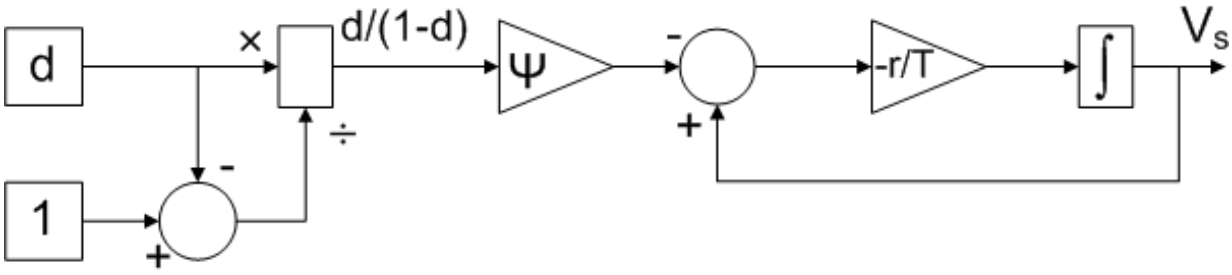

Figure 2.6: Control law block diagram.

The vibrometer used as a sensor for closing the control loop only supplies information about the beam tip velocity. Therefore, the controller will have the additional task of integrating $\dot{d}$ to obtain the beam tip position d. Figure 2.7 shows a block diagram representation of the actual controller circuit. It includes two additions to the previous block diagram, the first is an integrator at the beginning to convert the velocity signal from the vibrometer into displacement, and the second is for subtracting the controller voltage from the actuation voltage and multiplying the result by the voltage gain.

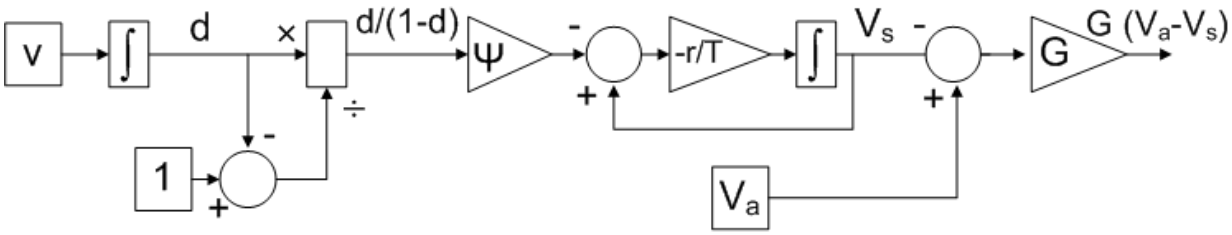

Figure 2.7: Actual controller block diagram.

2.4 Controller Blocks

The basic components of the controller shown in Figure 2.7 are:

- addition of two signals
- addition of a signal to a constant
- multiplication of a signal by a constant
- integration of a signal
- division of a signal by another signal

The implementation of all the previous operations is simple and straight forward except for integration of a signal and division of a signal by another.

2.4.1 Introduction to Op-Amps

Ideally, an Op-Amp (Figure 2.8) is a differential input, single output amplifier with an infinite gain [55]. It has two input nodes V_+ and V_- and one output node V_{out}. The governing equation of the amplifier is:

$$V_{out} = A(V_+ - V_-) \tag{2.15}$$

where A is the amplifier open-loop gain that is ideally infinite. The amplifier is driven through DC voltage supplies V_{cc+} and V_{cc-}. V_{out} is limited by the values of V_{cc+} and V_{cc-}, and any value outside this limit is clipped. If the output signal is totally outside that range, the Op-Amps is said to be *saturated*. Usually V_{cc+} and V_{cc-} are omitted from the diagram and the Op-Amp is presented as in Figure 2.9.

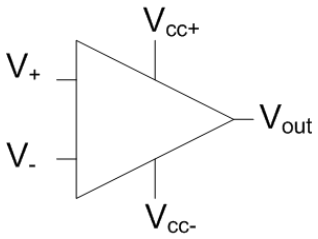

Figure 2.8: Op-Amp.

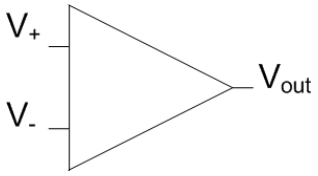

Figure 2.9: Op-Amp with power connections omitted.

When negative feedback is added to this ideal amplifier, reasonable gains that are independent of the infinite open-loop gain can be obtained. With other components (resistors, capacitors, etc.) connected around the Op-Amp with different combinations, many mathematical operations such as addition, subtraction, integration, and differentiation can be modeled.

As Op-Amps are not ideal devices, the open-loop gain in reality is both finite and frequency dependent. The gain value is usually in the range of $10^5 - 10^7$. The frequency dependence is due to the presence of parasitic capacitances. Each capacitor in parallel with a resistor introduces a pole in the system, thus making the whole device frequency

dependent. Op-Amps are typically internally compensated to act as a single-pole device according to the equation:

$$A(\omega) = A_0(\frac{1}{1+\frac{\omega}{\omega_c}}) \tag{2.16}$$

where A is the open-loop gain of the Op-Amp, A_0 is the open-loop gain at DC, ω is the input frequency, and ω_c is the cutoff frequency of the Op-Amp. At frequencies $\omega >> \omega_c$, the Op-Amp gain may be calculated as

$$A(\omega) = A_0(\frac{\omega_c}{\omega}) \tag{2.17}$$

thus decreases 20 dB every decade in frequency. The frequency at which the open loop gain A is equal to unity is called the Gain Bandwidth Product (GBP). For Op-Amps to operate close to the ideal, the GBP of the circuit should be less than that of the Op-Amp.

2.4.2 Multiplication by a constant

There are two main configurations for multiplication [55]:

- "inverting amplifier", Figure 2.10, where the non inverting input (V_+) is connected to ground, the input voltage is connected to the inverting input (V_-) through a resistor R_{in}, and a feedback resistor (R_f) is connected between the inverting input and the output of the Op-Amp.
- "non-inverting amplifier", Figure 2.11, where the inverting input (V_-) is connected to ground through a resistor (R_1), the input voltage is connected directly to the non-inverting input (V_+), and a feedback resistor (R_2) is connected between the inverting input and the output of the Op-Amp.

The amplifier can be used to multiply an input voltage V_{in} by a gain. For the inverting amplifier, the governing equation is

$$V_{out} = -\frac{R_f}{R_{in}}V_{in} \tag{2.18}$$

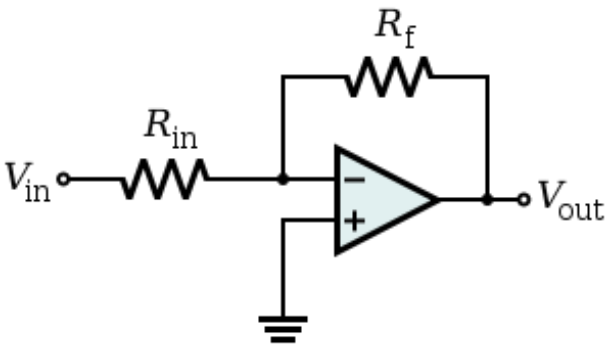

Figure 2.10: Inverting amplifier.

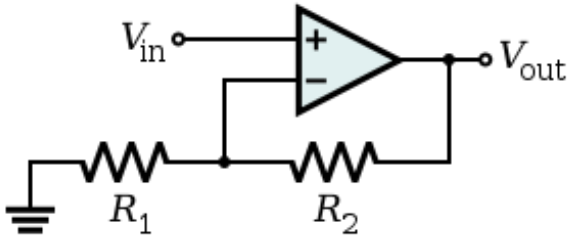

Figure 2.11: Non inverting amplifier.

and for the non inverting amplifier, the governing equation is

$$V_{out} = V_{in}(1 + \frac{R_2}{R_1}) \tag{2.19}$$

The advantage of the inverting amplifier is the simplicity, but it has the disadvantage of producing an inverted output. If the inverted output is not desired at the next stage, another inverting amplifier with a unity gain has to be added to get the desired output. On the other hand, the non-inverting amplifier is a bit more difficult to implement but it can save an unwanted additional stage [55].

2.4.3 Addition

The configuration shown in Figure 2.12 is used to add several weighted input voltages [55]. The governing equation for the circuit is

$$V_{out} = -R_f(\frac{V_1}{R_1} + \frac{V_2}{R_2} + ... + \frac{V_n}{R_n}) \tag{2.20}$$

In order to subtract an input voltage V_i, addition can be used after inverting V_i by using an inverting amplifier with both resistors equal $R_{in} = R_f$ [55].

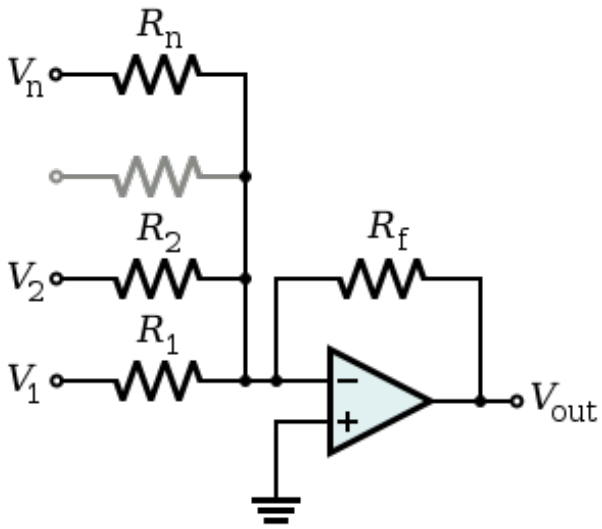

Figure 2.12: Addition using Op-Amps.

2.4.4 Signal Multiplication and Division

We use the identity

$$\ln(a) + \ln(b) - \ln(c) = \ln(\frac{a.b}{c}) \tag{2.21}$$

to implement multiplication and division of two signals. This is accomplished using a diode in the Op-Amp circuit. A diode is characterized by an exponential relation between the

current passing through it and the voltage difference between its terminals. The relation is given by

$$I_D = I_s(e^{\frac{V_D}{V_T}} - 1) \tag{2.22}$$

where, I_D is the current through the diode, V_D the voltage across its terminals, I_s the reverse saturation current, and V_T the thermal voltage. The reverse saturation current I_s and the thermal voltage V_T are constant characteristics of the diode.

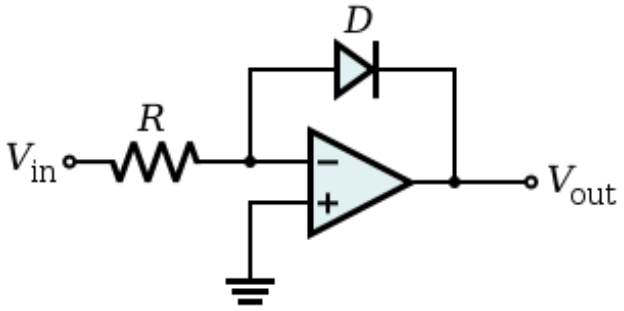

Figure 2.13: Logarithmic output Op-Amps circuit.

Thus in order to implement $\frac{v_1}{v_2}$, first we take the natural log of both signals, this is done using the configuration in Figure 2.13, where the output voltage is given by

$$V_{out} = -V_T \ln(\frac{V_{in}}{I_s R}) \tag{2.23}$$

We also have to take the natural log of an input of 1 volt. Then we add the outputs from v_1 and the 1 volt and subtract the output from v_2 (using similar Op-Amps so that the term $I_s R$ cancels out) to get

$$-[V_T \ln(\frac{v_1}{I_s R}) + V_T \ln(\frac{1}{I_s R}) - V_T \ln(\frac{v_2}{I_s R})] = -V_T \ln(\frac{v_1}{v_2 I_s R}) \tag{2.24}$$

Then the configuration in Figure 2.14, where $V_{out} = -RI_s e^{\frac{V_{in}}{V_T}}$, is used to get the final output as

$$V_{out} = -RI_s e^{\frac{-V_T \ln(\frac{v_1}{v_2 I_s R})}{V_T}} = \frac{v_1}{v_2} \tag{2.25}$$

Similarly, multiplication can be implemented by adding the natural log of the two signals and subtracting the natural log of an input of 1 volt then taking the exponent of the result [55].

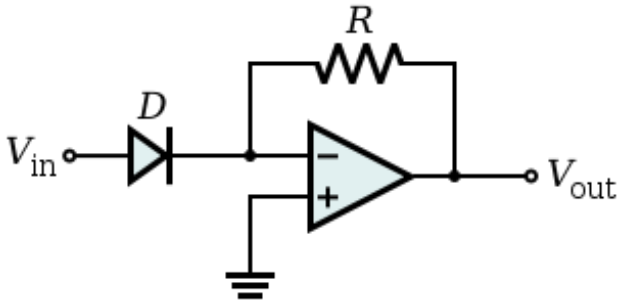

Figure 2.14: Exponential output Op-Amps circuit.

2.4.5 Integration

The standard integrator circuit [55] is shown in Figure 2.15 where

$$V_{out} = -\frac{1}{RC}\int V_{in}dt \tag{2.26}$$

The transfer function of the integrator in the Laplace domain is

$$\frac{V_{out}(s)}{V_{in}(s)} = -\frac{1}{sRC} \tag{2.27}$$

where s is the Laplace variable. Equation (2.27) gives a Bode plot of a line with a slope of -20 dB per decade in the amplitude plot and a line at -90^o in the phase plot. This means that for low frequency noise, a huge amplification in amplitude will take place, causing the Op-Amp to saturate. To overcome this problem, another resistor is connected in parallel to the capacitor, as shown in Figure 2.16, to act as a path for low frequency signals. As a result, the circuit changes from an integrator into a low pass filter and the transfer function of the system in the Laplace domain changes to

$$\frac{V_{out}(s)}{V_{in}(s)} = -\frac{R_2}{R_1}\frac{1}{1+R_2Cs} \tag{2.28}$$

Thus for frequencies higher than the cutoff frequency $\omega_c = \frac{1}{R_2 C}$ the low pass filter behaves as an integrator while at the same time the DC gain $G_{DC} = \frac{R_2}{R_1}$ is limited. Figure 2.17 shows the Bode plot of an integrator circuit in dashed line and a low pass filter circuit in solied line with $R_1 = 1k\Omega$, $R_2 = 10M\Omega$ and $C = 20nF$. For the low pass filter to function properly as an integrator, the input signal should be at least two decades higher than the cutoff frequency $\omega_c = 5rad/s$.

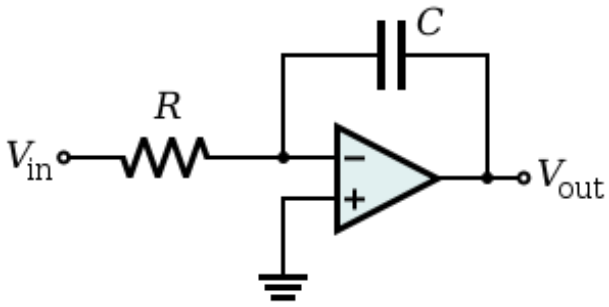

Figure 2.15: Op-Amp integrator circuit.

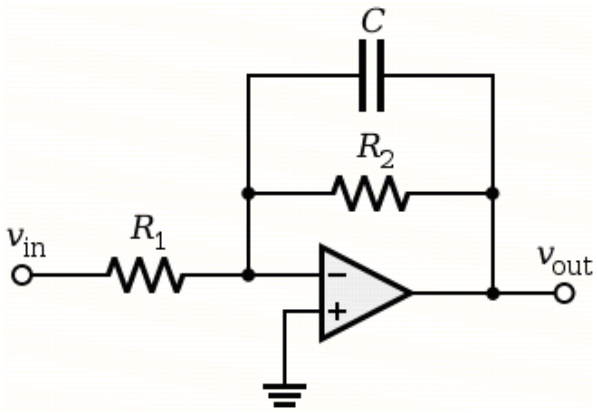

Figure 2.16: Low pass filter.

In all Op-Amps, there exists a DC voltage offset between the two input pins which is due to manufacturing imperfections. This DC offset shows as a small DC input voltage to the integrator and thus gets magnified by G_{DC} and shows at the output as a large DC

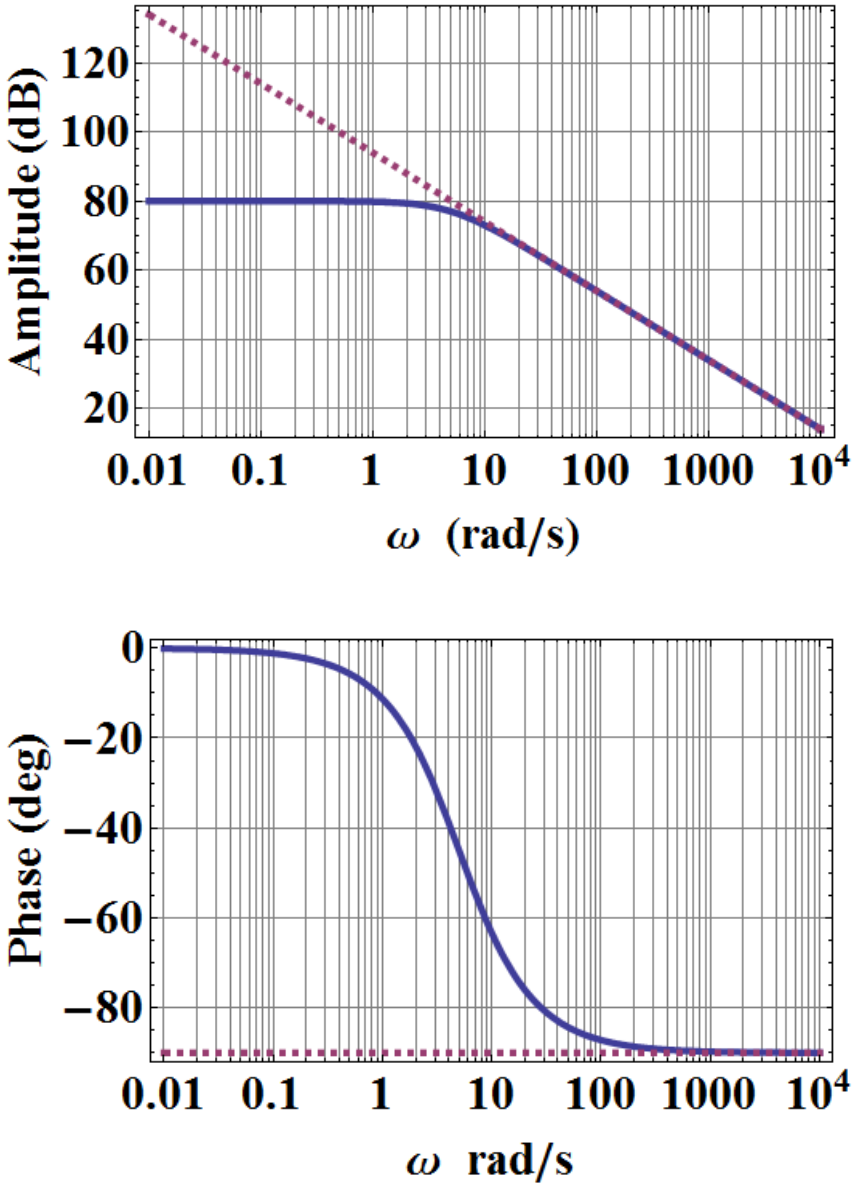

Figure 2.17: Bode plot of an integrator and a low pass filter.

voltage added to the signal. Even when using the low pass filter configuration, a relatively high DC gain exists. In the last example $G_{DC} = \frac{R_2}{R_1} = 10,000$, thus an offset of 1 mV will show as 10 V which will corrupt the output signal. To get rid of this DC voltage, a DC voltage that is equal to the offset but with opposite polarity is added to the input of the integrator. As the offset is not constant (may change over time from one test to another), the added amount should be controllable. A voltage divider circuit with a variable resistor is used to add this controlled voltage.

To be able to add a small DC voltage with positive and negative polarity, the two ends of the variable resistor are connected to two equal voltage sources with opposite polarities through large equal resistors. The middle leg is then connected to the input of the Op-Amp. By doing this, a controlled small voltage can be added to the input and tuned until a zero DC offset between the two input pins can be achieved [55]. Figure 2.18 shows the configuration used for nulling the offset. The values of $Rd1$,$Rd2$ and Rv control the range of voltages that can be added to the input. We can assume that no current flows to the Op-Amp, therefore V_v is calculated through voltage divisions as

$$V_v = 2V_+ \frac{Rd1 + Rv1}{Rd1 + Rd2 + Rv} - V_+ \tag{2.29}$$

where $Rv1$ is the resistance between the left and middle pin of the variable resistor and can take a value between $0 - Rv\Omega$. When $Rd1 = Rd2 = 100k\Omega$, $Rv = 2k\Omega$, and $V = 15V$, then the input voltage to the Op-Amp is within the range $V_v = [-0.1485V, 0.1485V]$.

2.5 Low and High-frequency Versions of the Controller

Two versions of the controller will be realized: one version will be integrated with a class of MEMS beams to create low-frequency actuators; the second version will be integrated with the same class of MEMS beams to create steady-state chaotic resonators. For the

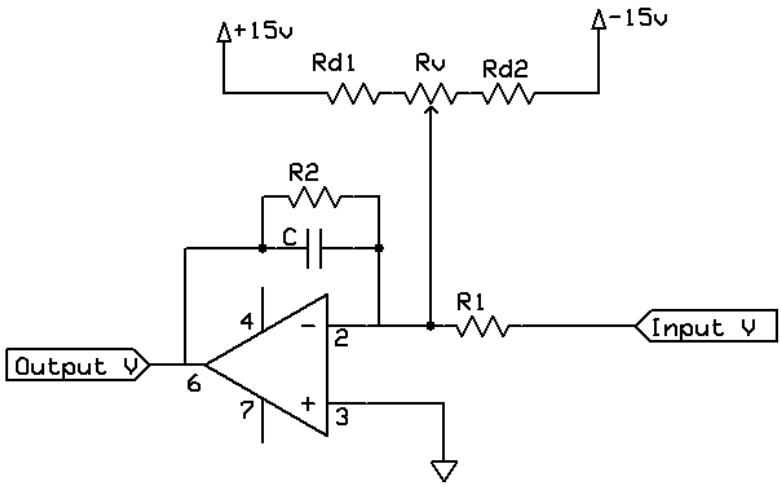

Figure 2.18: Voltage divider circuit connected to an integrator.

actuator, the system's operation should be either static or in low frequency (compared to the micro-beam's natural frequency). On the other hand, for the sensor, the system should operate dynamically at frequencies as high as the natural frequency of the micro-beam.

Two main sets of experiments are to be performed after integrating the controller into the system, namely low frequency tests and high frequency tests. The low frequency tests are intended to verify the use of the system as an actuator. On the other hand, high frequency tests are to validate the dynamic behavior and exploit the chaotic behavior of the system.

2.5.1 Actuator Controller

In Figure 2.6, the end feedback loop alone can be regarded as a linear system with an input $\Psi\frac{d}{1-d}$ and an output V_s. This system's transfer function is

$$T_f = \frac{\frac{r}{T}\frac{1}{s}}{1+\frac{r}{T}\frac{1}{s}} = \frac{1}{\frac{s}{r/T}+1} \tag{2.30}$$

which is a low pass filter with unit gain and a cutoff frequency at $\frac{r}{T}$. Given that the value of $\frac{1}{T}$ is greater than 50 kHz for the target beam class in this work, at slow operating frequencies this part of the block diagram reduces to a unit gain and can be removed. Therefore, the block diagram for the controller of the low frequency actuator is as shown in Figure 2.19

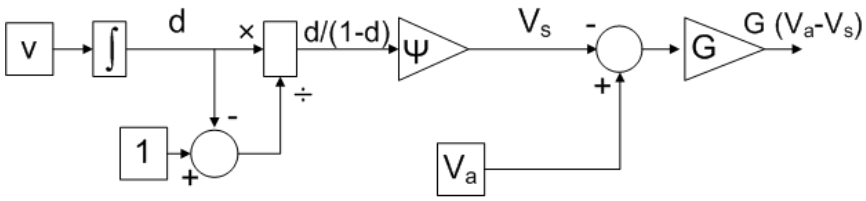

Figure 2.19: Block diagram of the controller operating at low frequencies.

In this case, the control law becomes

$$V_s = \Psi \frac{d}{1-d} \tag{2.31}$$

2.5.2 Chaotic Resonator Controller

The target micro-beam class natural frequencies are in the range of 60-120 kHz. As a result they requires high speed Op-Amps (high GBP) that can operate at these frequencies and supply a constant gain. In addition, at these high frequencies working on a bread-board can cause stability problems due to parasitic capacitances that arise from the bread-board itself and are significant only at high frequencies. Instead of a bread-board, a Printed Circuit Board (PCB) was designed and fabricated to suite the high frequency operation.

Chapter 3

Actuator Realization

3.1 Introduction

The objective of the actuator under design is to hold a desired static position while tracking a relatively low-frequency ω path around it. Driving the actuator using this harmonic command signal will produce a tip velocity of

$$v = A\omega \sin(\omega t) \tag{3.1}$$

where A is the amplitude the tip displacement. The nominal capacitor gap g is $2\mu m$. Assuming a travel range of 90% of the gap, yields a maximum travel of $1.8\mu m$. Therefore, a maximum displacement amplitude of $A_{max} = 0.9\mu m$ is reasonable. On the other hand, a vibrometer acquisition setting of 5mm/s/V limits the amplitude of the signal to 50mm/s. This means that for this setting, the maximum allowable frequency of operation is

$$f_{max} = \frac{50 \times 10^{-3}}{2\pi 0.9 \times 10^{-6}} = 8.8kHz \tag{3.2}$$

slightly higher frequencies can also be used when displacements are known to be limited to smaller values. If higher frequencies are to be used then the next higher acquisition setting (25mm/s/V) should be used.

3.2 Static analysis of the system

Equations (2.10)-(2.12) govern the dynamics of the close-loop system. For static analysis, the time derivatives are zero, which yields:

$$0 = v \tag{3.3}$$

$$0 = -\mu v + \frac{-c_3 d - c_4 d^2 - c_5 d^3 + c_6 G^2 (V_{DC}\sqrt{\alpha} - V_s)^2}{c_0 + c_1 d + d^2} \tag{3.4}$$

$$0 = -r(V_s - \frac{d}{1-d}\psi\sqrt{\alpha}) \tag{3.5}$$

where V_{DC} is the actuation voltage.

Substitute equations (3.3) and (3.5) into equation (3.4) to obtain:

$$c_5 d^3 + c_4 d^2 + c_3 d = c_6 G^2 (V_{DC}\sqrt{\alpha} - \frac{d}{1-d}\psi\sqrt{\alpha})^2 \tag{3.6}$$

which becomes, upon rearranging, a fifth-order polynomial in d. The polynomial has five solutions and potentially five equilibrium positions for every value of V_{DC}.

The equilibrium positions of the close-loop actuator for a voltage gain $G = 7$ and position gain $\Psi = 2$ are shown in Figure 3.1. The solid line is the locus of stable equilibrium positions and the dashed line is the locus of unstable equilibrium positions. One of the other three roots is aphysical, and the remaining two are complex conjugates. From the figure it can be seen that the actuator can reach a stable position as far as 90% of the gap.

Figure 3.2 shows an input voltage of $V_{in} = 10 + 10\sin(\omega t)V$ and the corresponding actuator response in simulation. It is clear that the beam tip follows the input signal and reaches more than 80% of the gap distance.

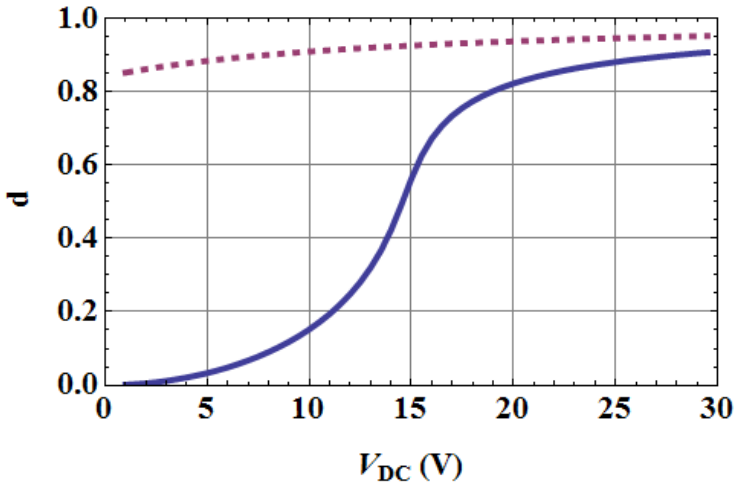

Figure 3.1: Equilibrium positions of the close-loop actuator where $G = 7$ and $\Psi = 2$.

Table 3.1: Micro-actuators dimensions.

	Nominal MA1	Nominal MA2	Identified MA2
L	150μm	120μm	128μm
w	20μm	20μm	20μm
h	2μm	2μm	1.9μm
g	2μ m	2μm	1.7μ m

3.3 Experimental Results

3.3.1 Test setup

Two micro-actuators, dubbed MA1 and MA2, were tested. The nominal dimensions of MA1 and MA2, as well as the experimentally identified dimensions of MA2, are listed in Table 3.1 [56].

The vibrometer was set to a dynamic range of 5mm/s/V. A function generator was used to generate the actuation voltage V_a and the controller was implemented on a bread-board.

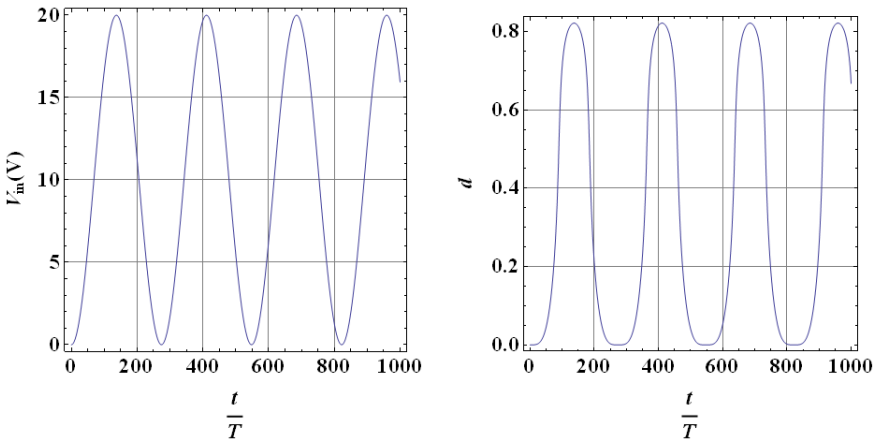

(a) Input voltage (b) Simulated beam tip displacement

Figure 3.2: Close-loop input voltage and simulated beam tip displacement.

Figure 3.3 shows the implemented controller on a bread-board.

3.3.2 Controller testing

Before closing the loop with the actual micro-beam, the controller was tested alone as a block. The controller testing was done for each major stage alone and then for the whole controller. During testing, the following values were used: integrator gain $\frac{1}{R_1 C} = 100$, $\Psi = 1$, and $G = 4.84$.

The integrator was tested using a sine wave input at two different frequencies. The output of the integrator was further multiplied by 25 to produce a total gain of 2500, which is needed to normalize the displacement as mentioned in section 2.2.3. For the first test a signal $V = 1\sin(\Omega t)V$ was used at a frequency of 1 kHz. Figure 3.4 shows the output of the integrator multiplied by 2500 for both simulation and experiment. For the second test, the input signal was $V = 4\sin(\Omega t)V$, at a frequency of 10 kHz. Figure 3.5 shows the output also multiplied by 2500 for both simulation and integration.

For testing the next stage of the controller, a voltage signal $d = 0.3 + 0.3\sin(\Omega t)V$ was

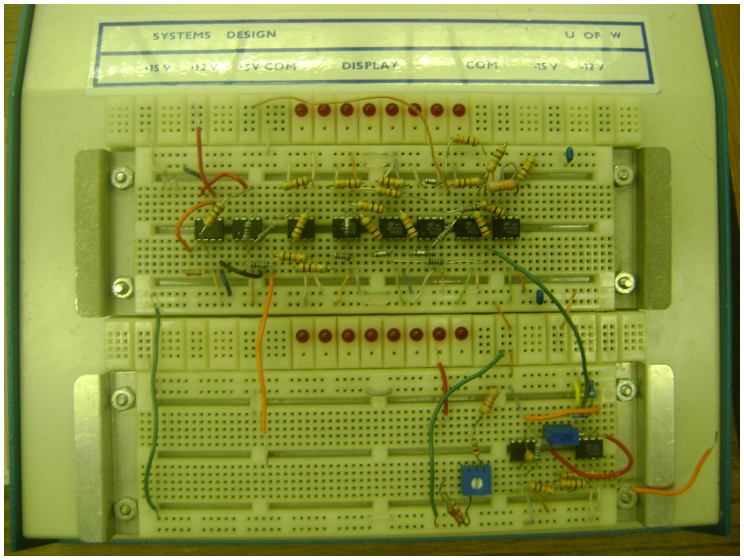

Figure 3.3: The controller implemented on a bread-board.

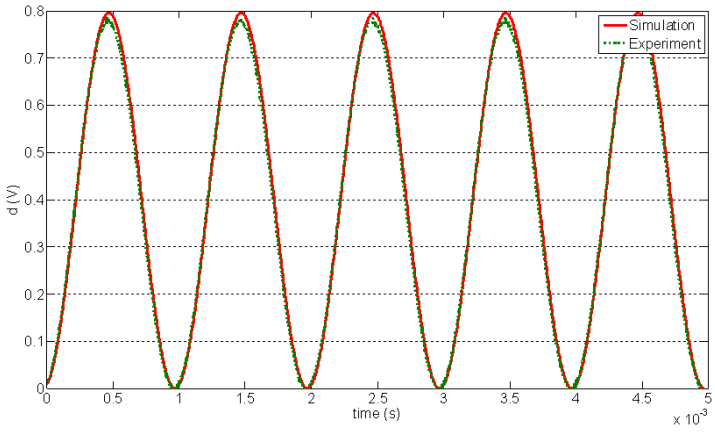

Figure 3.4: Integration output for a sine wave input.

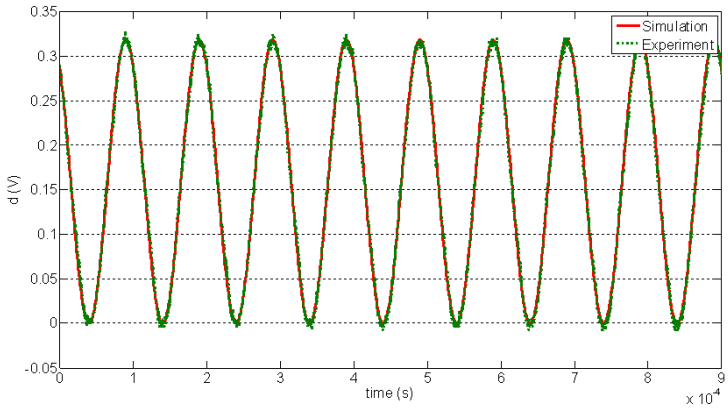

Figure 3.5: Integration output for a square wave input.

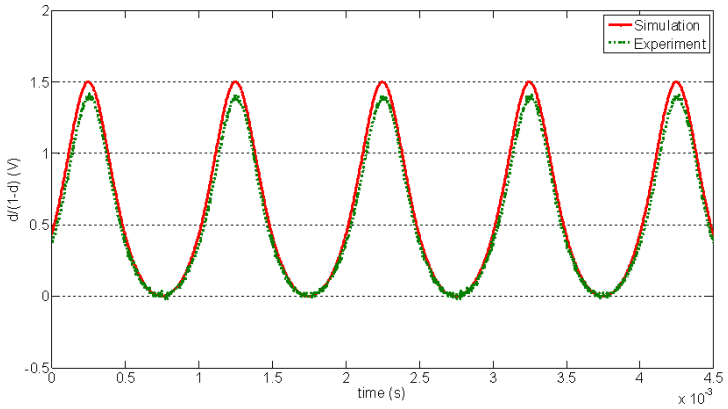

Figure 3.6: $\frac{d}{1-d}$ for an input signal $d = 0.3 + 0.3\sin(\Omega t)$ at 1kHz.

used to represent a displacement signal. Figure 3.6 shows $\frac{d}{1-d}$ in simulation and experiment for a frequency of 1 kHz.

Finally, the whole controller was tested for two different signals. For the first test, the input voltage was $v = 0.6\sin(\Omega t)V$ at 1 kHz and for the second test $v = 3\sin(\Omega t)V$. For both cases, an actuation voltage $V_a = 2\sin(\Omega t)V$ was used. Figures 3.7 and 3.8 show the displacement d, controller voltage V_s, and total voltage $G(V_a - V_s)$ for the first and the second test respectively.

3.3.3 Close-loop testing

Using the potentiometer mentioned in Section 2.4.5, the DC shift of the displacement signal can be adjusted. In the first close-loop tests, the system behaved properly only when the displacement signal was shifted to about half of the gap. Accordingly the control law is adjusted from equation [2.31] to

$$V_s = \Psi \frac{d+y}{1-(d+y)} \tag{3.7}$$

where y is the DC shift added to the nominal displacement signal.

After testing, we found that although the signal representing the displacement was seen as steady on the oscilloscope, it was actually riding on top of a low frequency noise signal. This noise signal was at 30 Hz with an amplitude of 0.5 V which corresponds to half the gap.

It was found that the vacuum pump used to hold the chip under the laser beam in the vibrometer is the source of this 30 Hz vibration. This vibration, after the integrator, appears as a sinusoidal signal with an amplitude of more than 0.5 V added to the displacement. Figure 3.9 shows the velocity (ch 1, orange) and displacement (ch 2, blue) with the vibrometer laser on but without driving the micro-beam. It can be seen clearly that there

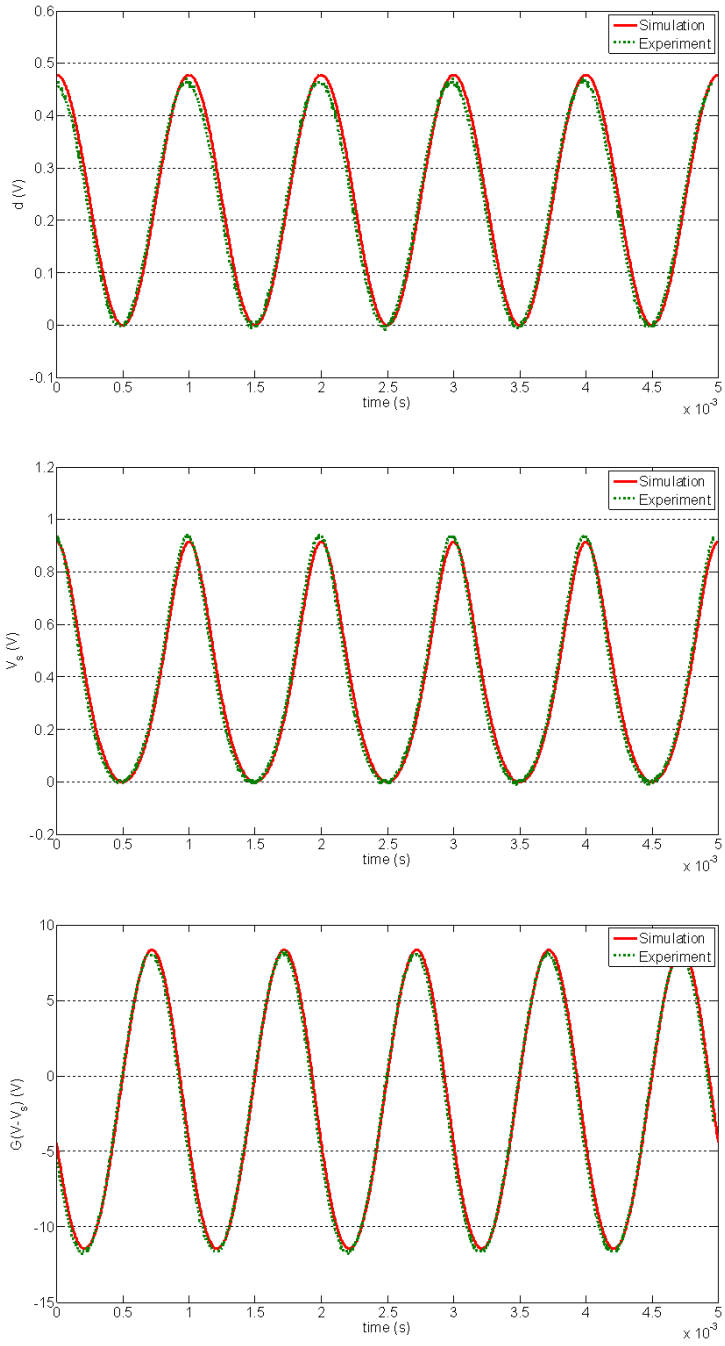

Figure 3.7: Controller outputs for an input signal $v = 0.6\sin(\Omega t)$ at 1 kHz.

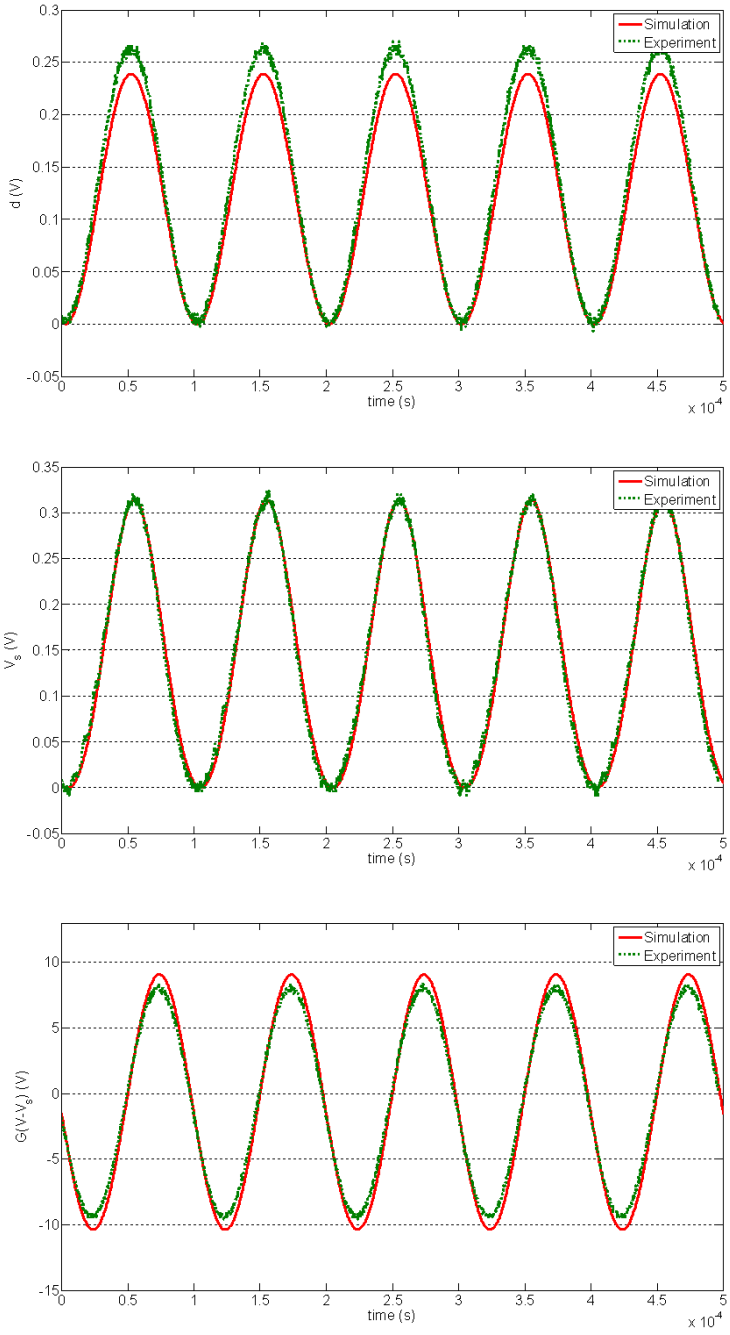

Figure 3.8: Controller outputs for an input signal $v = 3\sin(\Omega t)$ at 10 kHz.

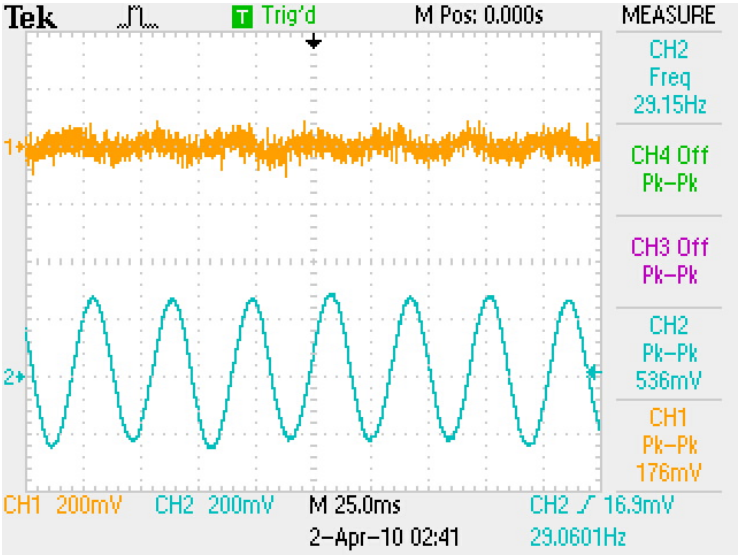

Figure 3.9: Velocity (orange) and Displacement (blue) without driving the micro-beam.

is an undesired noise signal at 30 Hz with amplitude that is equivalent to more than half the gap.

A second-order passive High-Pass-Filter was designed and implemented to remove this low frequency noise.

- Close-loop test results

After adding the HPF, the close-loop system was tested using an actuation voltage of $V_a = 2.5 + 2.5\sin[\omega t]$ at a frequency of 10 kHz. The voltage gain was set to $G = 4.8$ and the position gain was set to $\Psi = 0.5$. Simulation results were obtained by numerical integration of the system equations (2.10)-(2.12) using the actuator parameters identified experimentally for MA1.

Figure 3.10 shows the experimental and simulation results of the test. The results show good agreement between the model and experiment. The experimental displacement shows a travel range of more than 35% of the gap length which proves that the controller

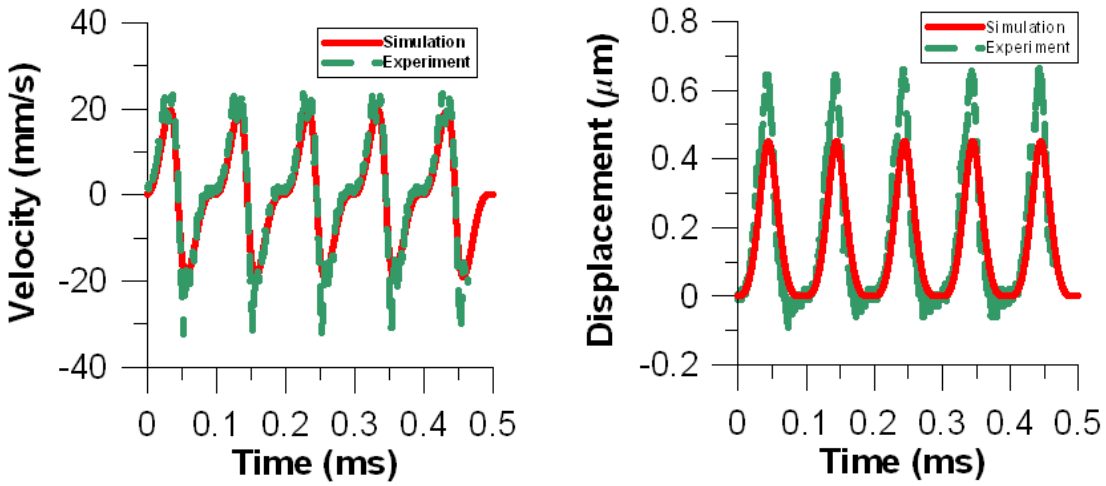

Figure 3.10: Experiment and simulation results for close-loop system at $V_a = 2.5 + 2.5\sin(\omega t)$, $\omega = 10kHz$, $G = 4.8$, and $\Psi = 0.5$.

successfully stabilized the system past the pull-in instability. Further resutls can be found in [1]

To get higher displacements, the vibrometer setting should be changed to the higher dynamic range of 25 mm/s/V.

Chapter 4

Sensor Realization

4.1 Introduction

Chaotic behavior is very sensitive to changes in the system parameters. As a result chaotic resonators are an attractive platform for highly sensitive detectors. In order to achieve this goal, three conditions should be satisfied. First, the resonator should be able to realize steady state chaotic behavior over a relatively large domain in the parameter space. Otherwise, small changes in the measurand will send the resonator out of the chaotic domain and sensing will fail. The second condition is that the system dynamics are clearly identified and understood so that the sensor can be easily calibrated. The third condition is the development of a calibration curve to relate changes in a specific system parameter to a metric of the chaotic attractor. The first two conditions are addressed in this work and the third will be addressed in future work.

Bifurcation diagrams are generated for four different AC voltage amplitudes while using the frequency as the control parameter. From the bifurcation diagrams, the best operating region is determined, and a complete picture for the dynamic behavior is obtained.

Table 4.1: Close-loop system parameters.

Parameter	Value
L	200μm
w	80μm
h	4.5μm
g	3μm
E	166 GP
μ	0.73
ρ	$2331kg/m^3$
r	100
c	$1.593 \times 10^{-}21$ Fm

4.2 System Setup

Equations (2.10)-(2.12) are used to represent the close-loop dynamic system. The system parameters used in these simulations are listed in table 4.1 [41].

Towfighian et al. [41] found that a region of bistability exist in the parameter space of the voltage and sensor gains G and Ψ. Bistability introduces rich dynamics to the system response and increases the likelihood of chaos. Figure 4.1 shows the static response of the close-loop actuator for $G = 0.8$ and $\Psi = 3$. The solid lines represent the locus of stable equilibria and the dashed lines represent the locus of unstable equilibria. At all voltage values the system has an equilibrium position that is aphysical ($d > 1$). In the range between $V_{DC} = 108V$ and $113V$ the actuator has four equilibrium positions, two of which are stable. Outside this range the system has one stable and one unstable equilibrium position.

In order to operate the actuator in the bi-stable region, the input voltage to the beam

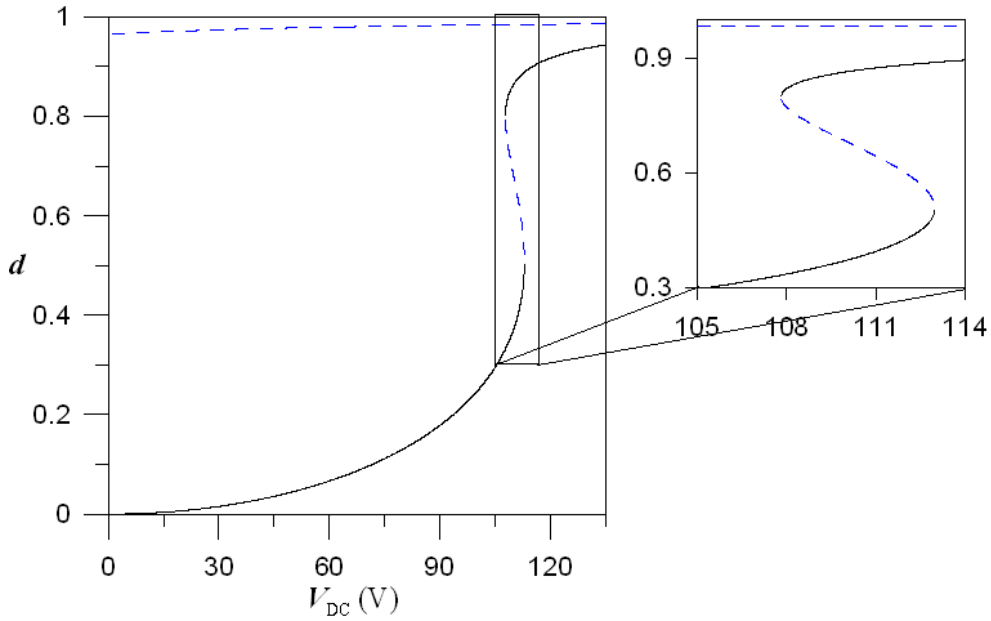

Figure 4.1: Static equilibria at $G = 0.8$ and $\Psi = 3$.

is set to $V = 110 + V_{AC}\cos(\omega t)$. The introduction of the AC voltage results in a harmonic force that destroys the stable foci and turn them into limit cycles around the equilibrium positions. A limit cycle is a closed curve in phase plane representing a periodic (oscillatory) motion. The equilibrium position around which the actuator oscillates is determined by the RMS value of the total actuating voltage. The equilibrium positions and corresponding natural frequencies for $V_{AC} = [2, 2.5, 3, 3.5]V$ are listed in Table 4.2.

4.3 Bifurcation Diagrams

A bifurcation is a qualitative change in the number of solutions and/or their stability as a system parameter changes. A bifurcation point is the location of this bifurcation in parameter space. Bifurcation diagrams are used to describe the evolution and relative position of system response (solution branches) as a function of a control parameter. They

Table 4.2: Stable positions and corresponding natural frequency.

V_{AC}	equilibrium position	natural frequency Ω_i	Stability
$2V$	0.371037	1.9742	Stable
	0.681634	0	Unstable
	0.863958	4.43694	Stable
	0.984587	43.6285	Unstable
$2.5V$	0.371144	1.97343	Stable
	0.681441	0	Unstable
	0.864018	4.44096	Stable
	0.984588	43.6302	Unstable
$3V$	0.371276	1.97250	Stable
	0.681206	0	Unstable
	0.864092	4.44586	Stable
	0.984588	43.6322	Unstable
$3.5V$	0.371432	1.97139	Stable
	0.680928	0	Unstable
	0.864092	4.44586	Stable
	0.984589	43.6345	Unstable

are constructed by stacking one-dimensional or two-dimensional Poincaré sections along an axis describing the progression of the control parameter. Poincaré sections describe the intersection of the system orbits in phase space with a lower-dimension object. They are either one-sided, where they record the intersection points as the orbit evolves from one side only to the other side of that object, or two-sided, where they record all intersections of the orbit with the object. In this work, we used the plane $v = 0$ as a Poincaré section. Accordingly, the value of d at the intersections with this section represent the maximum and minimum positions of the beam's tip. We used two-sided Poincaré sections because they allow us to describe both the existence and relative location of the orbit as well as its size.

The bifurcation diagrams were constructed using the following procedure:

1. At an excitation frequency ω away from the natural frequencies Ω_1 and Ω_2, long time integration was performed until the system settled on a stable period-one orbit. The numerical integration was carried out in Mathematica using the Modified Adams method. The Modified Adams method is a numerical method for integration that uses a Predictor-Corrector technique [57].

2. The states at an arbitrary point on the orbit were recorded and used as an initial guess (d_o, v_o, V_{so}) for the shooting method. The shooting method turns the problem of finding the closed orbits to a boundary-value problem where the initial and final points on the orbit after one period are matched. It then uses an initial-value solver to integrate the system equations for a period and interprets the difference between the initial and final point as an error to be corrected iteratively.

3. The shooting method was implemented by integrating the system equations starting from the initial guess for a period $T = \frac{2\pi}{\omega}$. The difference between the initial guess and the terminal point (d_f, v_f, V_{sf}) is then used to correct the initial guess until

the magnitude of the Euclidean norm of the error vector, the difference between the initial and terminal points on the orbit, is less than 10^{-3}.

4. The monodromy matrix of the obtained orbit was evaluated by integrating the system of equations augmented with the system of linearized perturbations around the orbit for a period starting from an initial condition on the converged orbit [43]. The monodromy matrix describes the growth or decay of perturbations to the initial point in each of the directions of phase-space as the system evolves along the orbit for one period.

5. The Floquet multipliers (the Eigenvalues of the monodromy matrix) were calculated. Floquet theory [43] was then used to determine the stability of the orbits, based on the values of those multipliers, and to determine the type of the bifurcation according to the following protocol

   - Orbits of non-autonomous system are stable when all multipliers lie inside the unit circle in complex plane.

   - The orbit undergoes a cyclic-fold bifurcation, if one of the Floquet multipliers leaves the unit circle through the point (1,0). At a cyclic-fold bifurcation a branch of stable orbits meets a branch of unstable orbits and they both vanish.

   - The orbit undergoes a period-doubling bifurcation, if one of the Floquet multipliers leaves the unit circle through the point (-1,0). There are two types of period-doubling bifurcations, supercritical and subcritical. In both cases, a stable branch of orbits looses stability at the bifurcation point. In supercritical period-doubling bifurcations, a branch of stable period-doubled orbits is created at the bifurcation point. In a subcritical period-doubling bifurcations, a branch of unstable period-doubled orbits vanishes at the bifurcation point.

6. The excitation frequency was incremented to a larger or smaller value depending on

the sweep direction and a point on the converged orbit at the previous frequency was used as the initial guess for the shooting method.

7. Steps 3-6 were repeated until the tracked orbit lost stability.

   - Where stability was lost through a period-doubling bifurcation, steps from 2 to 6 were repeated and the period of integration was doubled.

   - Where stability was lost through a cyclic-fold bifurcation, steps from 1 to 6 were repeated while searching for a new set of orbits.

8. Unstable orbits were tracked where relevant.

9. For every orbit, the intersections with the zero-velocity line ($v = 0$) were recorded, thus the bifurcation diagram represents a set of two-sided Poincaré sections. A period-one orbit is represented by two points, a period-two orbit is represented by 4 points, etc.

10. The bifurcation diagram was then constructed by stacking the Poincaré sections as a function of the excitation frequency. Since the increment in frequency is small, these discrete points appear as continuous lines. For unstable orbits, one of ten points was plotted in order to appear as dotted lines.

11. Because motion within a chaotic attractor is aperiodic, the shooting method fails there. Instead, long-time integration was used and the intersections with the zero-velocity line were recorded after at least one hundred periods to allow for the transient response to decay.

4.3.1 Lyapunov exponent

The Lyapunov exponents are calculated to verify the existence of and to characterize the chaotic attractors. The Lyapunov exponent is a measure of expansion or contraction of

perturbations around a given trajectory. It is an asymptotic quantity defined locally in state space. Quantitatively, if two trajectories start close to each other in state space with an initial separation of δs, then the evolution of the distance between them can be described by

$$|\delta s(t)| \approx e^{\lambda t}|\delta s(t)| \tag{4.1}$$

where λ is the Lyapunov exponent. The rate of contraction or expansion depends on the orientation of the initial perturbation. Any dynamic system has a number of Lyapunov exponents equal to its order. A dissipative system, where phase-space is contracting, becomes chaotic when at least one Lyapunov exponent is positive [43] indicating the presence of an exponentially growing process inside the contracting space.

Nayfeh and Balachandran [43] present an algorithm to calculate the Lyapunov exponents for autonomous systems. Since our system is non-autonomous, we transformed it into an autonomous system by replacing the explicit time dependence ωt in equation [2.11] with a new state variable θ and adding a state equation describing its evolution to the system:

$$\dot{d} = v \tag{4.2}$$

$$\dot{v} = -\mu v + \frac{-c_3 d - c_4 d^2 - c_5 d^3 + c_6 G^2(\sqrt{\alpha}(V_{DC} + V_{AC}\cos\theta) - V_s)^2}{c_0 + c_1 d + d^2} \tag{4.3}$$

$$\dot{V_s} = -r(V_s - \frac{d}{1-d}\Psi\sqrt{\alpha}) \tag{4.4}$$

$$\dot{\theta} = \omega \tag{4.5}$$

To calculate the Lyapunov exponents, the following steps were followed:

1. The system equations were augmented with the system of linearized perturbations around the orbit $y(t)$, and integrated for a period of time T_f. The initial conditions of the dynamic system were chosen arbitrarily while the initial conditions of the linearized perturbations system $y(0)$ were set equal to the identity matrix.

2. The vectors $y_1(T_f)$, $y_2(T_f)$, $y_3(T_f)$, and $y_4(T_f)$ were obtained from the columns of $y(T_f)$.

3. A new set of vectors was obtained by orthonormalizing the set $y_i(T_f)$ using the Graham-Schmidt procedure:

$$\hat{y}_1 = \frac{y_1(T_f)}{||y_1(T_f)||} \tag{4.6}$$

$$\hat{y}_2 = \frac{y_2(T_f) - (y_2(T_f).\hat{y}_1)\hat{y}_1}{||y_2(T_f) - (y_2(T_f).\hat{y}_1)\hat{y}_1||} \tag{4.7}$$

$$\hat{y}_3 = \frac{y_3(T_f) - (y_3(T_f).\hat{y}_2)\hat{y}_2 - (y_3(T_f).\hat{y}_1)\hat{y}_1}{||y_3(T_f) - (y_3(T_f).\hat{y}_2)\hat{y}_2 - (y_3(T_f).\hat{y}_1)\hat{y}_1||} \tag{4.8}$$

$$\hat{y}_4 = \frac{y_4(T_f) - (y_4(T_f).\hat{y}_3)\hat{y}_3 - (y_4(T_f).\hat{y}_2)\hat{y}_2 - (y_4(T_f).\hat{y}_1)\hat{y}_1}{||y_4(T_f) - (y_4(T_f).\hat{y}_3)\hat{y}_3 - (y_4(T_f).\hat{y}_2)\hat{y}_2 - (y_4(T_f).\hat{y}_1)\hat{y}_1||} \tag{4.9}$$

   where (X.Y) denotes the dot product.

4. The augmented system was integrated again for a period T_f while using the state values at $t = T_f$ as initial conditions for the system equations, and $\hat{y}_i$ vectors as initial conditions for the linearized perturbations. After the integration, the y_i vectors are orthonormalized using the Graham-Schmidt procedure.

5. The Lyapunov exponents were calculated as

$$\lambda_i = \frac{1}{rT_f} \sum_{k=1}^{r} \ln N_i^k \tag{4.10}$$

   where N is the norm in the denominator of $\hat{y}_i$, the subscript i refers to the ith vector, the superscript k refers to the iteration number, and r is the total number of iterations.

6. Steps 2-4 were repeated until the values of the Lyapunov exponents asymptotically converged.

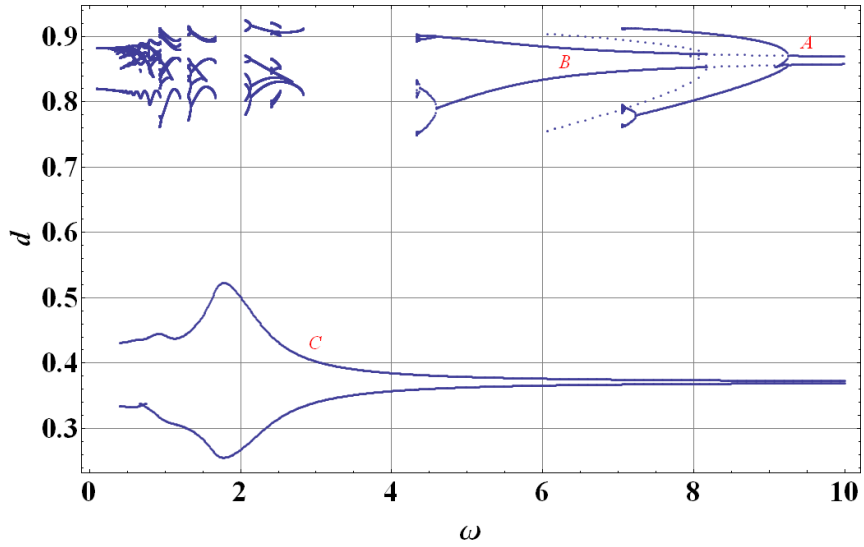

Figure 4.2: Bifurcation diagram for $V_{AC} = 2V$.

The Lyapunov exponents were calculated for large branches of chaotic attractors. The value of the maximum Lyapunov exponent was used to verify the existence of chaos and to measure the relative activity of the chaotic attractor.

4.3.2 Excitation amplitude $V_{AC} = 2V$

Figure 4.2 shows the bifurcation diagram for an AC amplitude of $V_{AC} = 2V$ where solid lines represent stable orbits and dotted lines represent unstable orbits. The effect of the two potential wells is obvious in the appearance of orbits limited to the lower well and others limited to the upper well. No two-well orbits were observed at this excitation level.

In the upper well, Figure 4.3, orbits undergo significant qualitative changes. Starting at $\omega = 10$ and sweeping the frequency down, a branch of stable period-one orbits exists in the upper well, this branch will be dubbed branch A. The stable period-one orbit loses stability due to a supercritical period-doubling bifurcation at $\omega = 9.245$. Beyond the period-doubling bifurcation, a stable period-two orbit coexists with an unstable period-

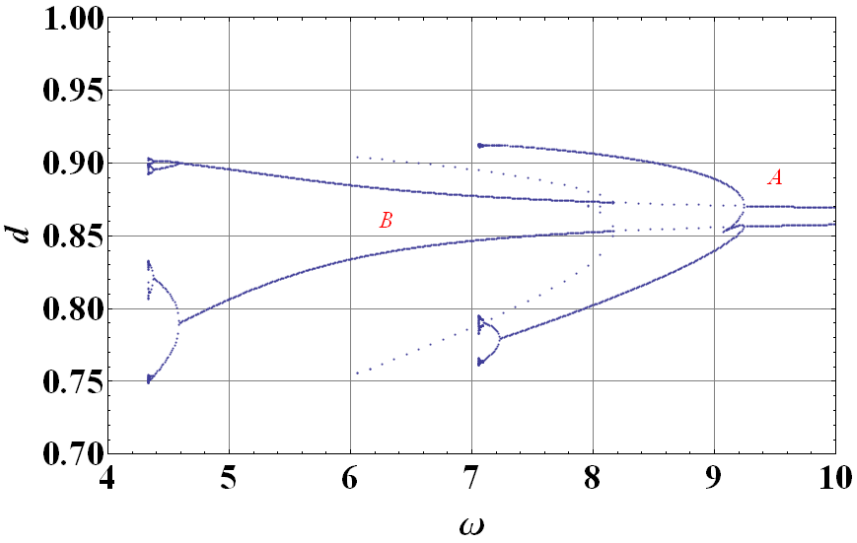

Figure 4.3: Upper well orbits for $V_{AC} = 2V$.

one orbit. As shown in Figure 4.4, the period-two orbit deforms as the frequency decreases and intersects the zero-velocity line only twice per period. The reason for this anomaly is that the response of the system at $\frac{\omega}{2}$ continues to grow as the frequency decreases until it dominates the response at $\omega = 9.07$. As a result, each cycle sees only two velocity reversals and appears in the bifurcation diagram as two points instead of four.

The stable period-two orbit originating from the previous bifurcation undergoes a cascade of period-doubling bifurcations leading to chaos. Period four appears at $\omega = 7.231$ and chaos starts at $\omega = 7.065$.

The period-one unstable orbit originating from branch A regains stability through a subcritical period-doubling bifurcation at $\omega = 8.165$ where a new branch of stable solutions, dubbed branch B, starts. This stable period-one orbit coexists with an unstable period-two orbit born at the bifurcation point as well as the stable orbits of branch A described above. Sweeping down in frequency, branch B experiences a cascade of supercritical period-doubling bifurcations leading to chaos. Period-two orbits appear on the branch at $\omega =$

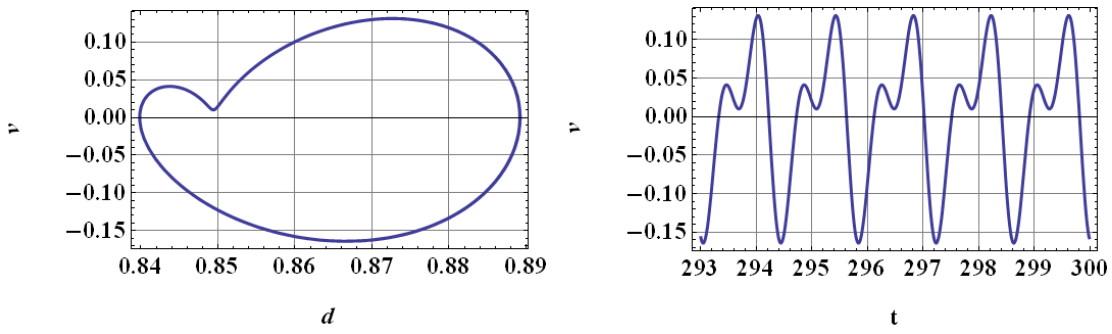

Figure 4.4: Phase portrait and time profile of velocity for a period-two orbit at $V_{AC} = 2V$ and $\omega = 9$.

4.589, period-four orbits appear at $\omega = 4.374$, and chaos appears at $\omega = 4.344$.

Still in the upper-well, but at low frequencies, Figure 4.5, another set of branches exist. The first branch (blue) starts from a cyclic-fold bifurcation at $\omega = 2.833$. Figure 4.6 shows the phase portrait and FFT plot for an orbit on this branch at $\omega = 2.2$. The orbit shows a superharmonic resonance of the order two. This can be deduced from the FFT of the orbit. The dominant peak is present at twice the excitation frequency. This orbit experiences a cascade of supercritical period-doubling bifurcations leading to chaos. Period-two orbits start at $\omega = 2.132$, period-four orbits start at $\omega = 2.061$, and chaos starts at $\omega = 2.05$.

Coexisting with the previous orbits is a set of period-two periodic orbits (red) that appears at $\omega = 2.53$ from a cyclic-fold bifurcation. Figure 4.7 shows the phase portrait of both orbits. The two orbits look as if they intersect, but that is only because the figure is a 2-D projection of the 3-D phase space (d, v, V_s). The period-two orbits experience superharmonic period-doubling bifurcation at $\omega = 2.419$ and then goes through a cascade of period-doubling bifurcations ending with chaos at $\omega = 2.045$.

Similarly, superharmonic orbits of order three (yellow) and four (green) are observed in the neighborhood of $\omega = \frac{\Omega_2}{3}$ and $\omega = \frac{\Omega_2}{4}$. These orbits appear through a cyclic-fold bifurcation and disappear through a cascade of period-doubling bifurcations and chaos.

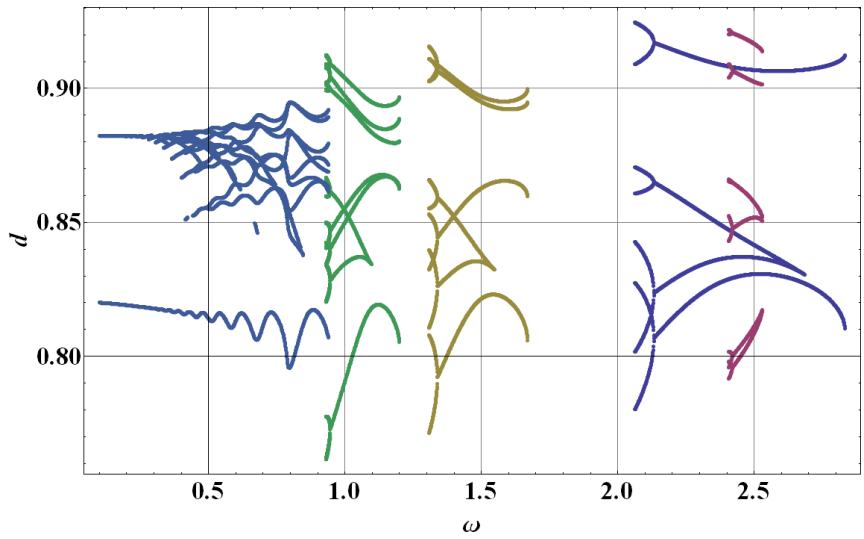

Figure 4.5: Bifurcation diagram showing superharmonics at the upper well at $V_{AC} = 2V$.

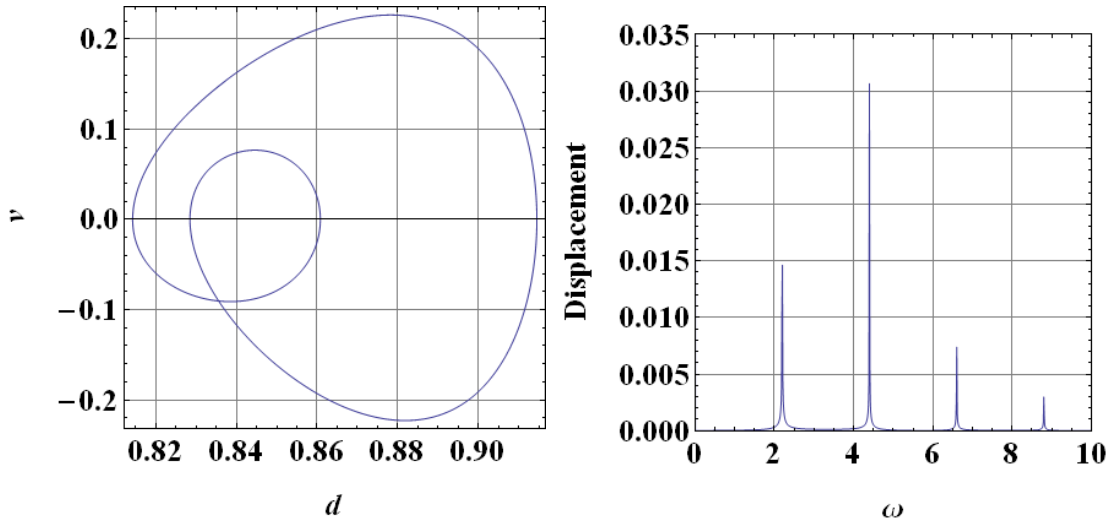

Figure 4.6: Phase portrait and FFT plot of an orbit at $\omega = 2.2$ and $V_{AC} = 2V$.

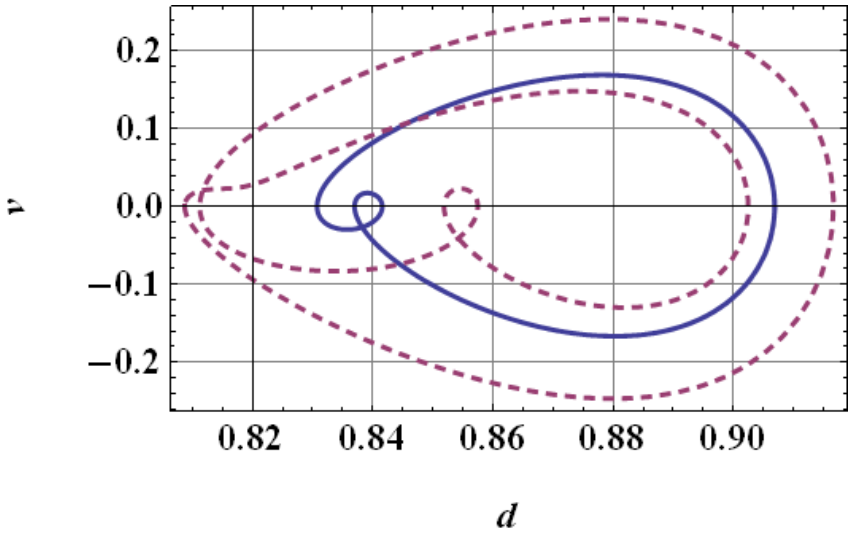

Figure 4.7: Phase portrait at $\omega = 2.5$ and $V_{AC} = 2V$ for different initial conditions leading to coexisting orbits.

The last branch of orbits (blue) is born through a cyclic-fold bifurcation at $\omega = 0.94$ and produces superharmonic orbits of higher order. Due to the small spacing between these superharmonic orbits, no boundaries appear between them.

It is obvious from Figure 4.5 that the region of existence of superharmonic orbits in frequency decreases as the order of superharmonic increases.

On the other hand, no qualitative change takes place in the lower well orbits and there is only a dynamic amplification in the response in the neighborhood of the natural frequency of the lower equilibrium position Ω_1, see Figure 4.2. This branch of orbits starting from $\omega = 10$ will be called branch C.

4.3.3 Excitation amplitude $V_{AC} = 2.5V$

Figure 4.8 shows the bifurcation diagram for an AC amplitude $V_{AC} = 2.5V$. In the upper well, branches A and B are qualitatively similar to those appearing at $V_{AC} = 2V$. Starting

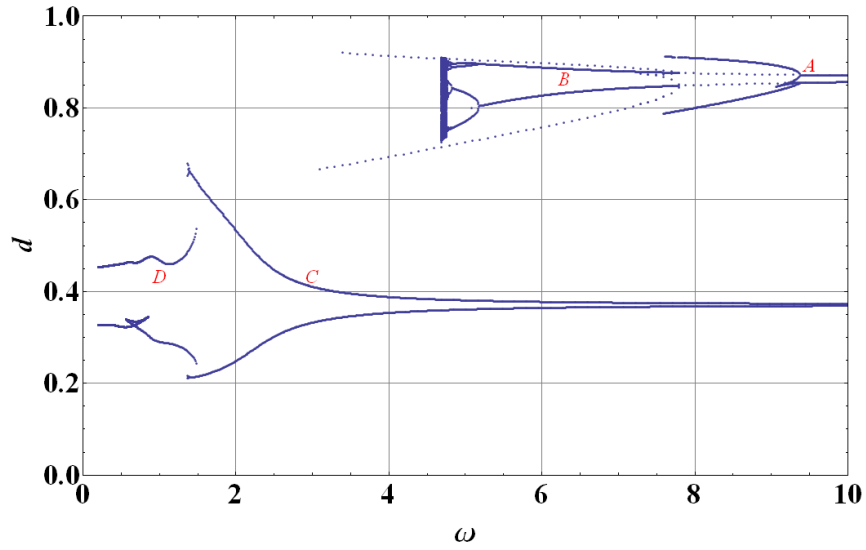

Figure 4.8: Bifurcation diagram for $V_{AC} = 2.5$.

from $\omega = 10$, a branch of stable period-one orbits exists and looses stability through a supercritical period-doubling bifurcation at $\omega = 9.37$. As before, a cascade of period-doubling bifurcations takes place and ends with chaos. Branch B starts at $\omega = 7.79$. Again, this branch looses stability through a supercritical period-doubling bifurcation that occurs at $\omega = 5.09$ and then experiences a cascade of period-doubling bifurcations ending with chaos at $\omega = 4.76$.

Figure 4.9 shows the bifurcation diagram of the chaotic region. The chaotic region spans a significantly larger region than the case with the $V_{AC} = 2V$ excitation. This is primarily due to its existence farther from the lower-well resonance and thus having enough energy in the upper-well. The chaotic attractor experiences an interior crisis at $\omega = 4.76$, after which is expands in size.

In the lower well new dynamics appear around the natural frequency of the lower equilibrium position. Branch C splits into two branches, C at high frequencies and D at low frequencies. For branch C, starting from $\omega = 10$ and sweeping down in frequency, a

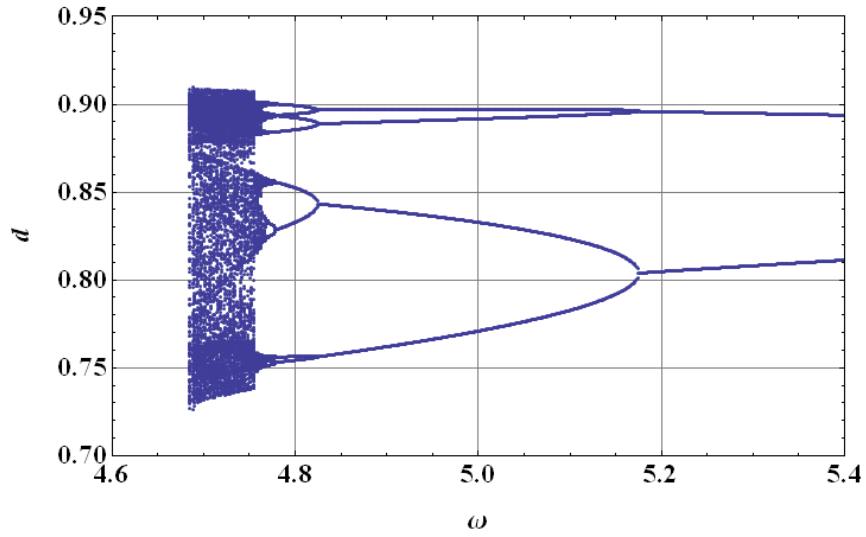

Figure 4.9: Bifurcation diagram for chaos in the upper-well at $V_{AC} = 2.5V$.

cascade of period doubling bifurcations takes place. Period-two orbits start at $\omega = 1.385$, period-four at $\omega = 1.363$, period-eight at $\omega = 1.359$, and chaos at $\omega = 1.352$, see Figure 4.10. Only the period-two orbit branch is shown due to the very small span of higher-order orbits.

Branch D starts through a cyclic-fold bifurcation at $\omega = 1.48$, thus coexisting with part of the other branch of period one orbits and with all its higher-order orbits. Sweeping down, these orbits do not experience any qualitative change except for the appearance of superharmonic resonances in the region between $\omega = 0.55$ and 0.86.

The behavior of the system in Figure 4.10 indicates a softening-type system. Figure 4.11 shows a typical softening-type bifurcation diagram where two branches of stable orbits exist. The two stable orbits coexist over a region and they both lose stability in a cyclic-fold bifurcation. In our system, period-doubling bifurcations and chaos occurred due to the presence of the controller which suppresses the orbit's size expansion.

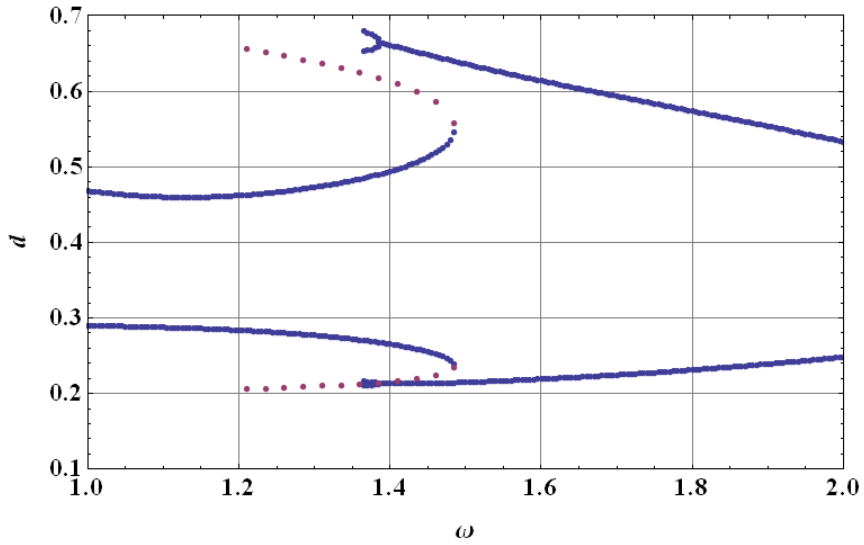

Figure 4.10: Inset of Figure 4.8.

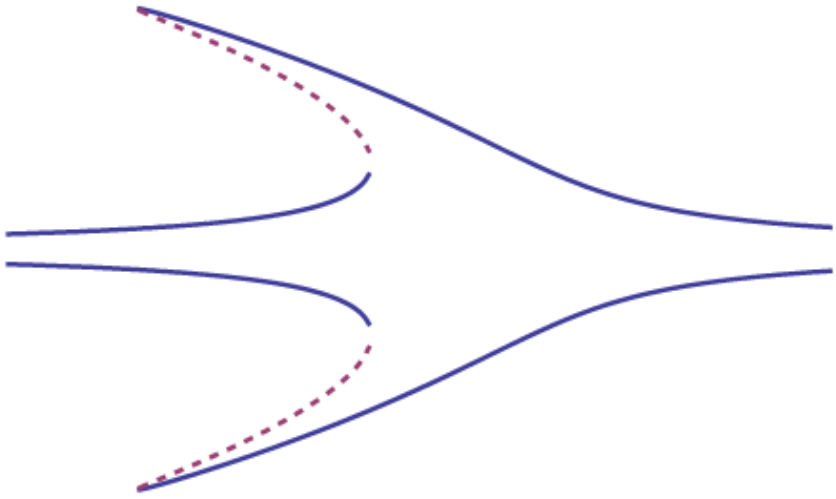

Figure 4.11: Softening-type bifurcation diagram.

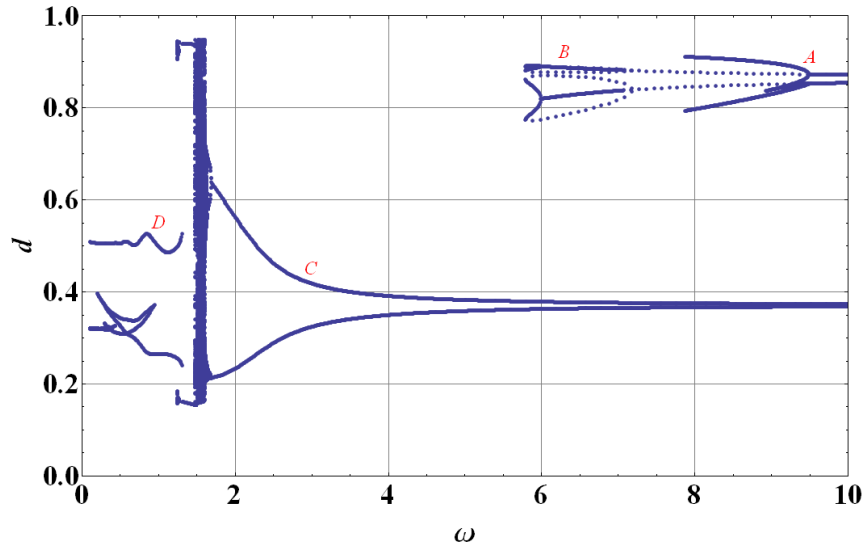

Figure 4.12: Bifurcation diagram for $V_{AC} = 3V$.

4.3.4 Excitation amplitude $V_{AC} = 3V$

At an AC amplitude of $V_{AC} = 3V$, Figure 4.12, minor changes occur in the upper-well orbits while major changes occur in the lower-well orbits. For the upper well, it can be observed that the period-two stable branch originating at the supercritical period-doubling bifurcation at $\omega = 6$ meets the branch of unstable orbits originating from the subcritical bifurcation at $\omega = 7.1$ and both orbits vanish in a cyclic fold bifurcation. Following the same trend, the region of existence of the stable period-one orbits of branch B decreased more. For branch A, chaos was observed around $\omega = 7.7$.

As for the lower well, branch C goes through a cascade of period-doubling bifurcations that ends with chaos. Period-two orbits start at $\omega = 1.69$, period-four orbits start at $\omega = 1.643$, period-eight orbits start at $\omega = 1.634$, and chaos starts at $\omega = 1.632$. The chaotic region of grew significantly compared to the chaotic region at $V_{AC} = 2.5$. Figure 4.13 shows the bifurcation diagram of the chaotic region. The chaotic region starts with a banded chaotic attractor that exists primarily in the lower well with occasional excursions

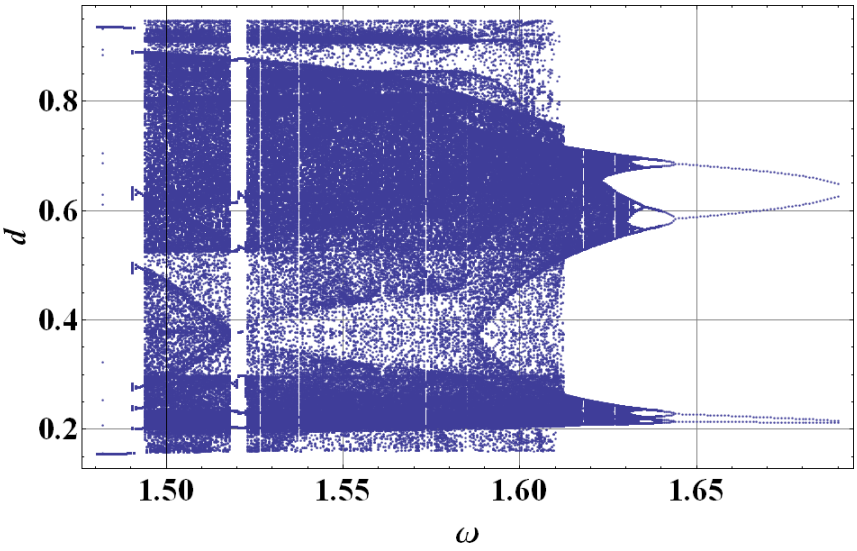

Figure 4.13: Bifurcation diagram of the lower well chaotic attractor at $V_{AC} = 3V$.

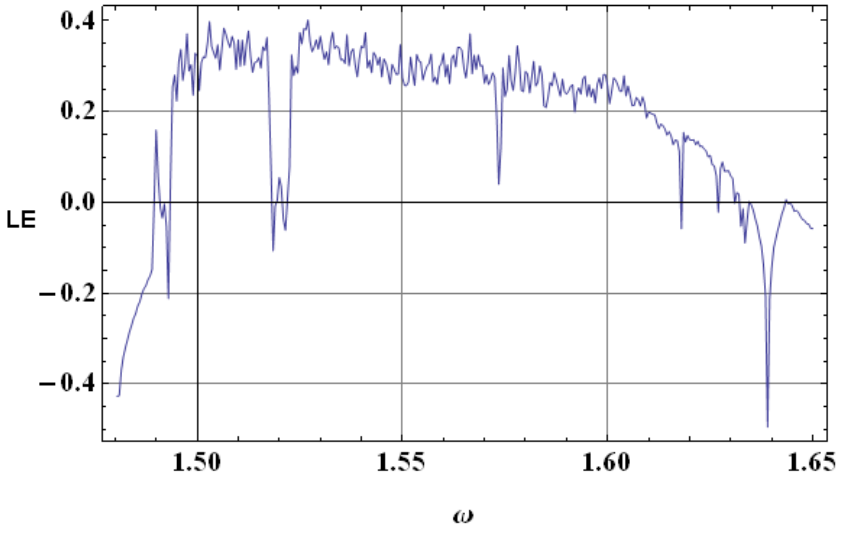

Figure 4.14: Maximum Lyapunov exponent for the chaotic region at $V_{AC} = 3V$.

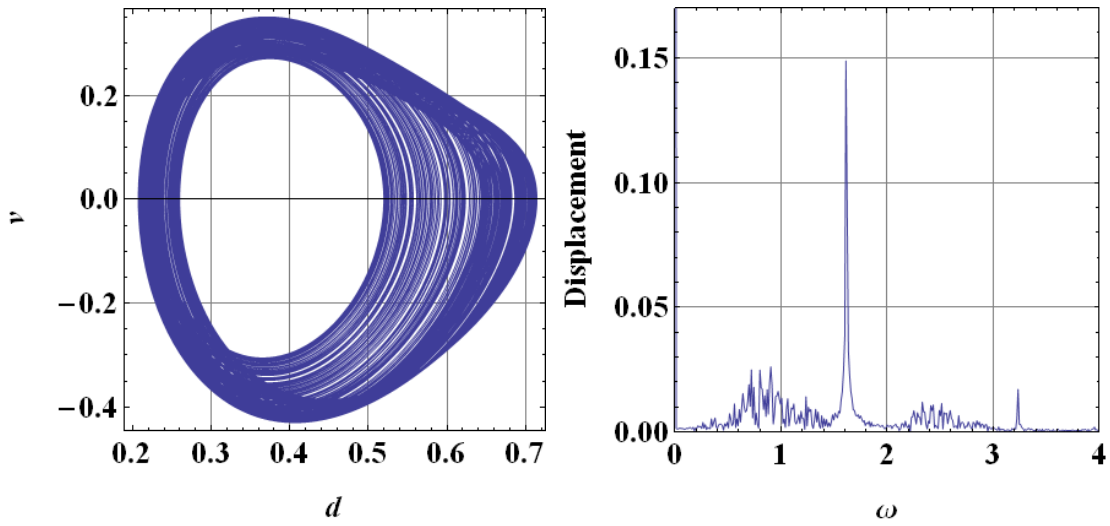

Figure 4.15: Phase portrait and FFT plot of banded chaotic attractor at $\omega = 1.615$ and $V_{AC} = 3V$.

over the saddle. Figure 4.15 shows the phase portrait and FFT plot of an attractor at $\omega = 1.615$. The broadband character of the orbit's frequency spectrum is a distinguishing characteristic of chaotic solutions [43]. The attractor expands abruptly to a two-well fully-developed chaotic attractor at $\omega = 1.612$ after experiencing an interior crisis. Figure 4.16 shows the phase portrait and FFT plot of a fully developed attractor at $\omega = 1.615$.

The white spaces inside the attractor are periodic windows. A period-six window appears at $\omega = 1.627$, a period-five window at $\omega = 1.618$, a period-four window at $\omega = (1.585, 1.574, 1.522)$, and a period-three window at $\omega = 1.493$. This sequence of periodic windows was experimentally observed by Simoyi et al. [58] in chemical reactions. Figure 4.17 shows the return map constructed from the phase portrait at $\omega = 1.615$ using a one sided Poincaré section at $v = 0$. The map is uni-modal in accordance with theory stating that any system that goes through period doubling sequence would have dynamics similar to the 1D map [58].

Figure 4.14 shows the maximum Lyapunov exponent for the region $\omega = [1.45 - 1.65]$.

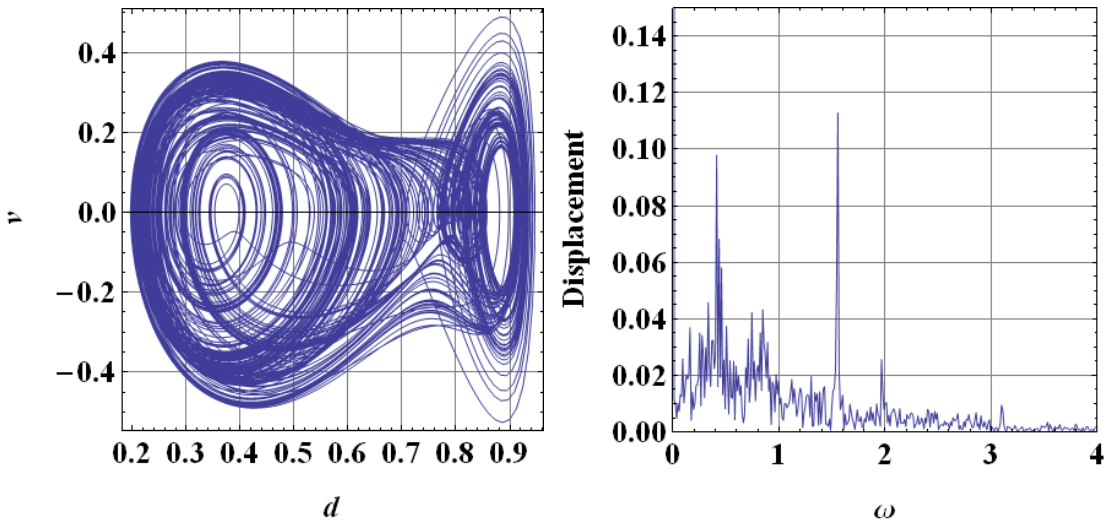

Figure 4.16: Phase portrait and FFT plot of a fully developed chaotic attractor at $\omega = 1.55$ and $V_{AC} = 3V$.

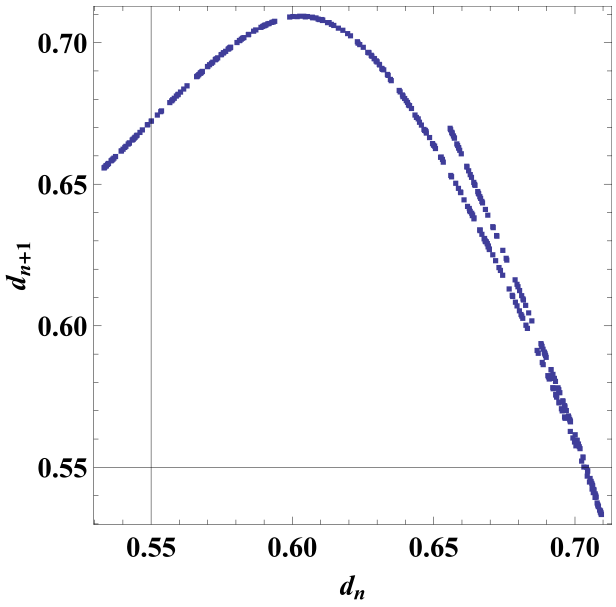

Figure 4.17: The uni-modal return map of the chaotic attractor at $\omega = 1.615$.

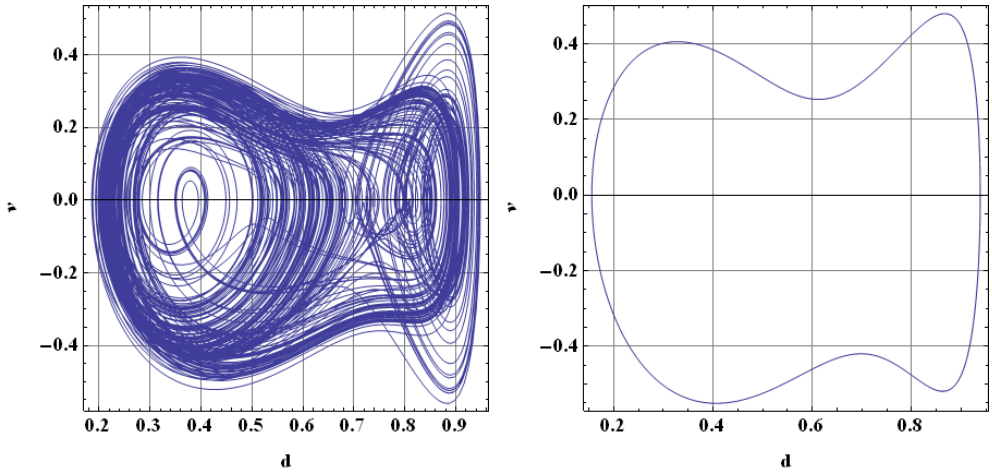

Figure 4.18: Transient chaos at $\omega = 1.442$ and $V_{AC} = 3V$.

The Lyapunov exponent is negative for the periodic orbits preceding that chaotic region, zero at bifurcation points, and positive at chaotic attractors. The figure shows that chaos starts at $\omega = 1.632$, grows with increasing the size of the attractor, and then settles after reaching the full-size of the attractor. The downward spikes inside the chaotic region are caused by the chaotic windows.

The chaotic attractor ends at $\omega = 1.494$ after colliding with an unstable branch in a boundary crisis. In its place appears transient chaos which settles down onto a two-well period-one stable orbit. In the transient chaos region, chaotic behavior for more than 200 exciting period then settles onto the two well periodic orbit. Figure 4.18 shows the phase portrait at $\omega = 1.442$ before and after settling to the two well orbit.

The two-well period orbit appears from a cyclic fold bifurcation at $\omega = 1.493$. Sweeping the frequency down, the two well stable orbit goes through a cascade of period doubling bifurcations ending with banded chaos.

Again, branch D appears at low frequencies coexisting with the two-well chaotic region, see Figure 4.20. Figure 4.19 shows a chaotic attractor coexisting with a stable one-well orbit in the lower well at $\omega = 1.25$.

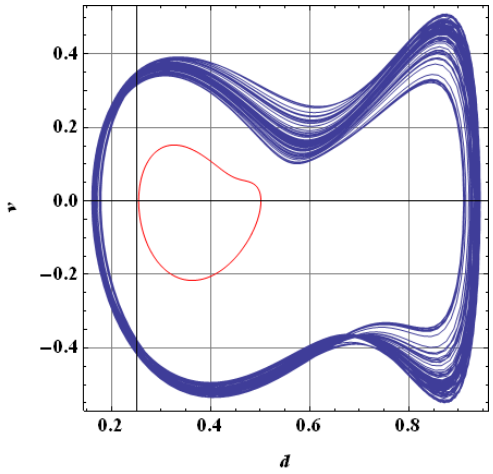

Figure 4.19: Two-well banded chaos coexisting with a one-well stable orbit at $\omega = 1.25$ and $V_{AC} = 3V$.

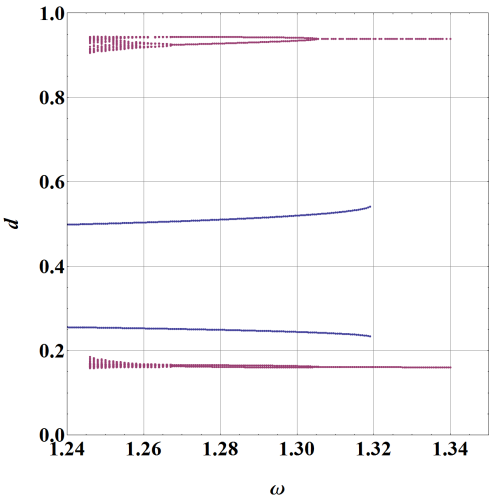

Figure 4.20: Coexistence of two-well branch of orbits and chaos with a stable one-well periodic orbit.

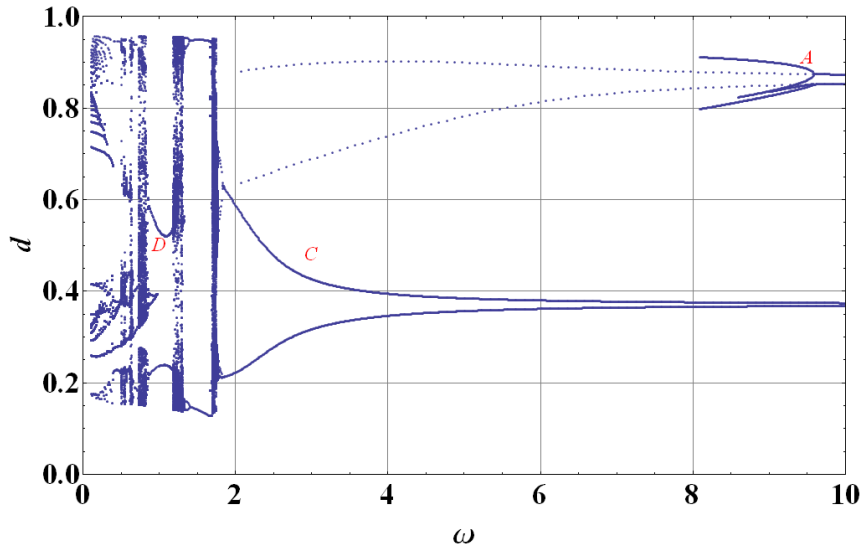

Figure 4.21: Bifurcation diagram for $V_{AC} = 3.5$.

4.3.5 Excitation amplitude $V_{AC} = 3.5V$

Figure 4.21 shows the bifurcation diagram at an excitation amplitude of $V_{AC} = 3.5V$. Branch A continues to exist in the upper well. It starts with a stable period-one orbits that lose stability in a supercritical period-doubling bifurcation as seen before. The stable period-two orbits born at this bifurcation experience a cascade of period-doubling bifurcations culminating in chaos. As before, chaos appears in a very small region of the frequency spectrum and is very difficult to observe due to its proximity to pull-in. On the other hand, the branch of unstable period-one orbits does not regain stability and, as a result, branch B disappears from the bifurcation diagram.

In the lower well, the banded chaotic attractor, primarily residing in the lower-well, still exists but starts at a higher frequency and exists over a smaller frequency range. On the other hand, the banded two-well chaotic attractor expands and becomes even wider in frequency than the primarily one-well chaotic region. Figure 4.22 shows an inset of the bifurcation diagram showing both primarily one-well and two-well chaotic attractors.

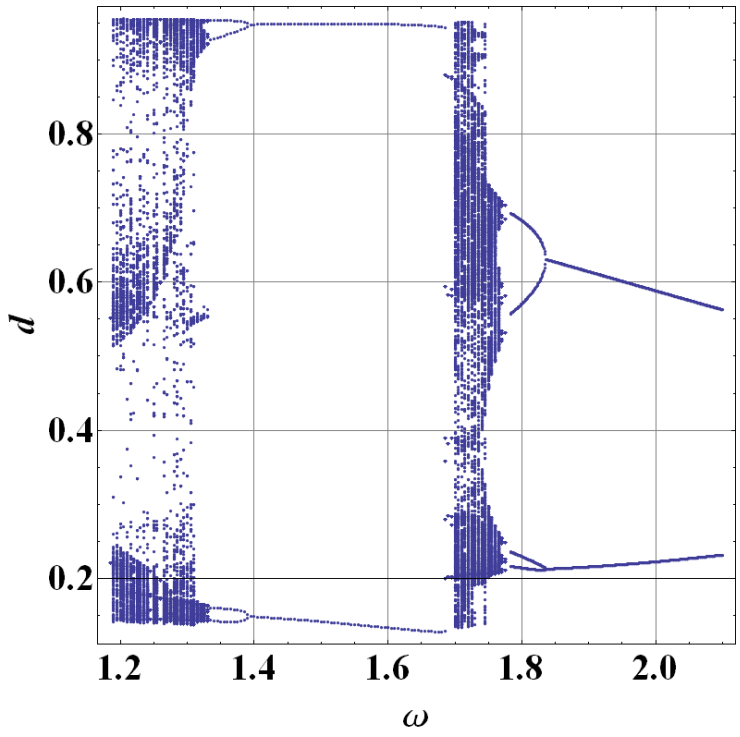

Figure 4.22: Bifurcation diagram for chaotic regions at $V_{AC} = 3.5V$.

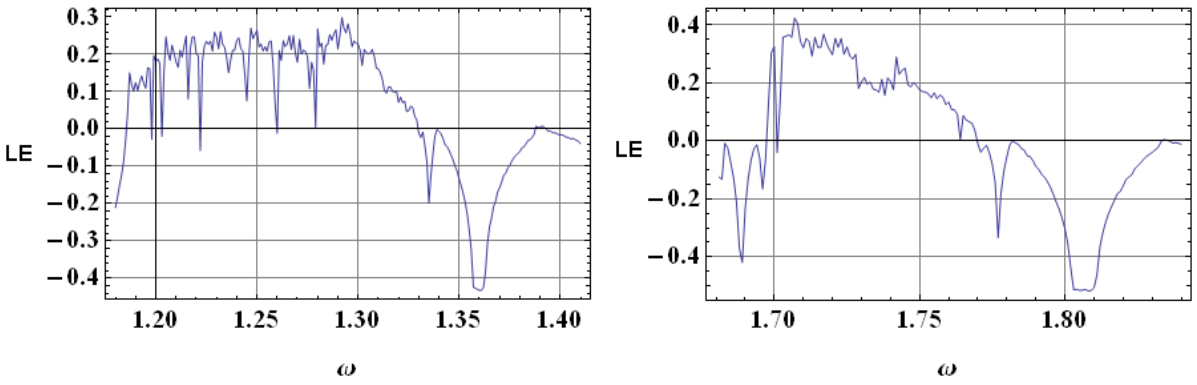

Figure 4.23: Maximum Lyapunov exponent for chaotic attractors at $V_{AC} = 3.5V$.

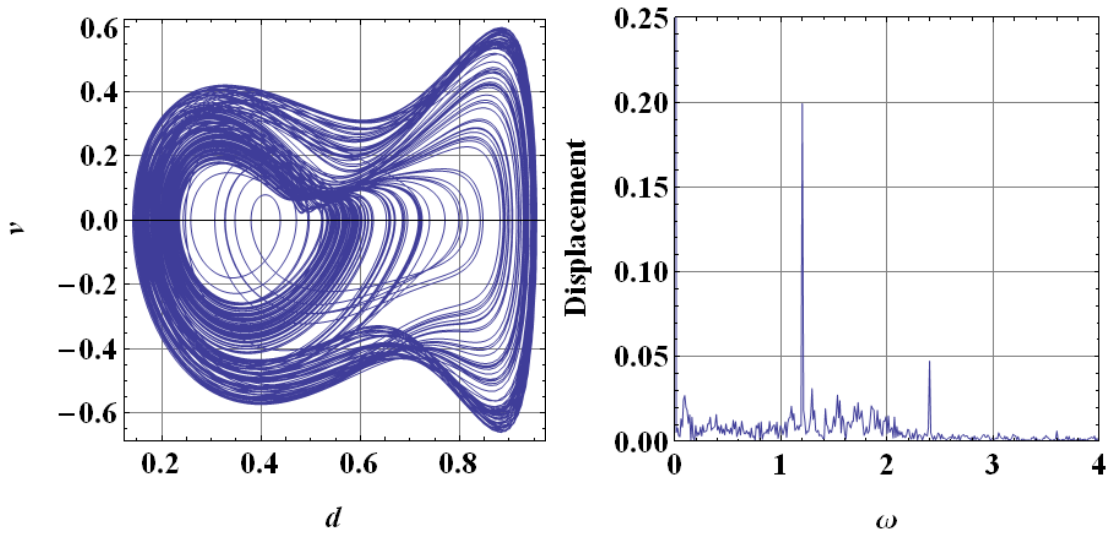

Figure 4.24: Phase portrait and FFT plot of a two-well chaotic attractor at $\omega = 1.2$ and $V_{AC} = 3.5$V.

Figure 4.24 shows the phase portrait and the FFT of a two-well chaotic attractor at $\omega = 1.2$.

Figure 4.23 shows the maximum Lyapunov exponent for the two chaotic attractors in figure 4.22. From the FFT and Lyapunov exponents plots, it can be seen that fully developed two-well chaotic attractor evolving from the banded one-well chaotic attractor is more active than the one evolving from the banded two-well chaotic attractor. The maximum Lyapunov exponent for the first reaches 0.4, while for the second it only reaches 0.3.

Orbits on branch D appear at lower frequencies and experience period-doubling bifurcations to chaos. Figure 4.25 shows the a zoom in on the bifurcation diagram from $\omega = 1.2$ to $\omega = 0.1$.

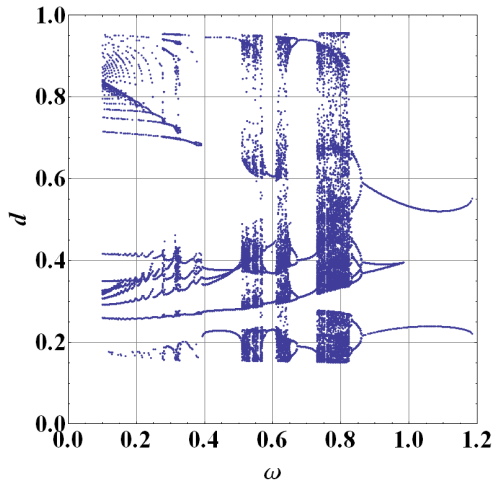

Figure 4.25: Bifurcation diagram for superharmonic orbits at $V_{AC} = 3.5V$.

4.4 Analysis of the Chaotic Attractors

Steady-state chaotic attractors are present at all the excitation levels considered. The availability of steady-state chaos over a wide range in parameter space is requirement in order to use chaos in sensing application. All the upper well branches of chaotic attractors cover narrow bands in frequency domain and are too close to the pull-in instability, rendering them bad choices as operating regions. On the other hand, the branch of primarily lower-well chaotic attractors and the branches of two-well chaotic attractors, where they are available, cover wider bands in frequency domain and are located farther away from the pull-in instability.

The bandwidth of the branch of primarily one-well chaotic attractors increases as the excitation amplitude increase from $V_{AC} = 2.5V$ to $V_{AC} = 3V$ then decreases as the excitation amplitude continues to increase from $V_{AC} = 3V$ to $V_{AC} = 3.5V$. Thus the maximum bandwidth of the primarily one-well branch exists in the neighborhood of $V_{AC} = 3V$. On the other hand, the bandwidth of the two branches of fully-developed two-well chaotic attractors increase consistently with the forcing amplitude. The two-well branches have

the advantage of wider bandwidth, while the primarily one-well branch has the advantage of operating away from the pull-in instability. The bifurcation diagram for $V_{AC} = 4V$ are presented in [56].

To further investigate the long-time behavior of the chaotic attractors, the basin of attraction of selected chaotic attractors were generated. They confirm the availability of a wide basin of attraction that assures system robustness. Figure 4.26 shows the basin of attraction for a banded primarily one-well chaotic attractor at $V_{AC} = 3$ and a frequency of $\omega = 1.62$. This figure was constructed by dividing the phase space into a grid of initial conditions while holding $V_s[0] = 0$ then starting long time integration from each grid point. After one hundred integration periods, the system settled on an orbit and the maximum position in the last two integration periods was recorded. The basin of attraction was then plotted as a grid where the color intensity decreases with the recorded position.

Inside the potential wells, the initial conditions are well mixed due to the action of the chaotic attractor. Outside the wells, all initial conditions go to pull-in. Therefore, the basin of attraction of the chaotic attractor encompasses a wide region in phase space comprising the two potential wells. Figure 4.27 shows the basin of attraction for a two-well chaotic attractor at $V_{AC} = 3$ and a frequency of $\omega = 1.62$. The similarity between the basin of attraction of both figures ensures robustness of both chaotic attractors.

In contrast to the previous figures, Figure 4.28 shows the basin of attraction of three coexisting stable orbits at $V_{AC} = 2V$ and $\omega = 7.5$. The orbit on branch A and pull-in appear in a light hue. The orbit on branch B appears in a slightly darker hue. The orbit on branch C appears dark. The basin of attraction shows the separation of initial conditions as the stable and unstable manifolds deform.

As a conclusion, operating in the two-well chaotic region is preferred when the system operation requires a wide frequency range and at the same time working in a low noise environment. On the other hand, the one-well chaotic region would be preferred in

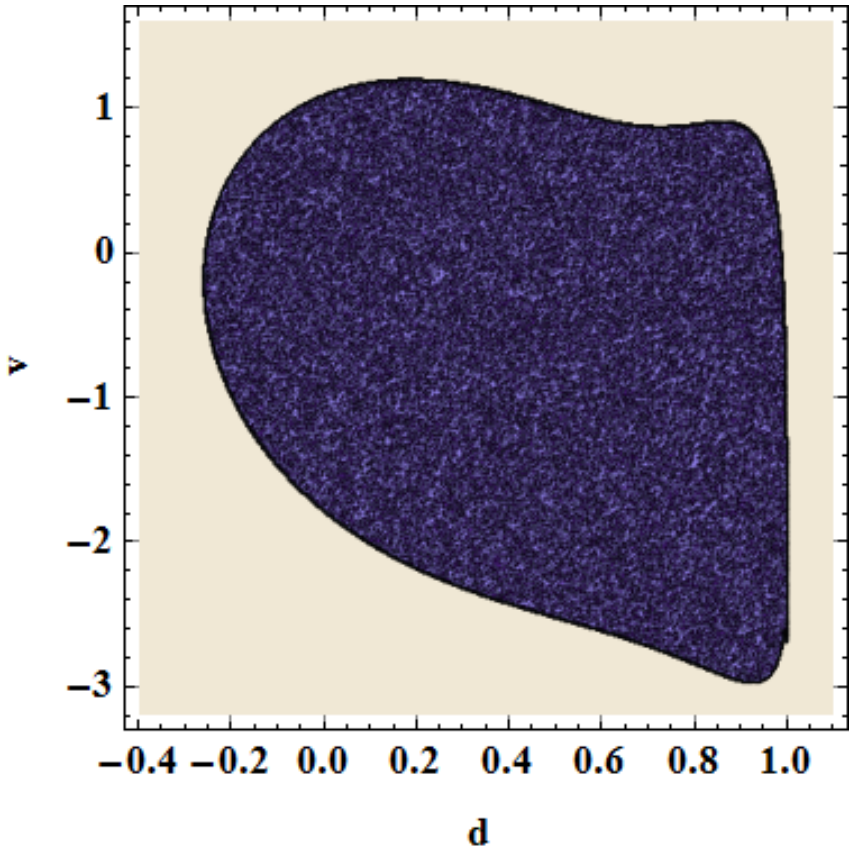

Figure 4.26: Basin of attraction of chaotic attractor at $\omega = 1.62$ and $V_{AC} = 3V$.

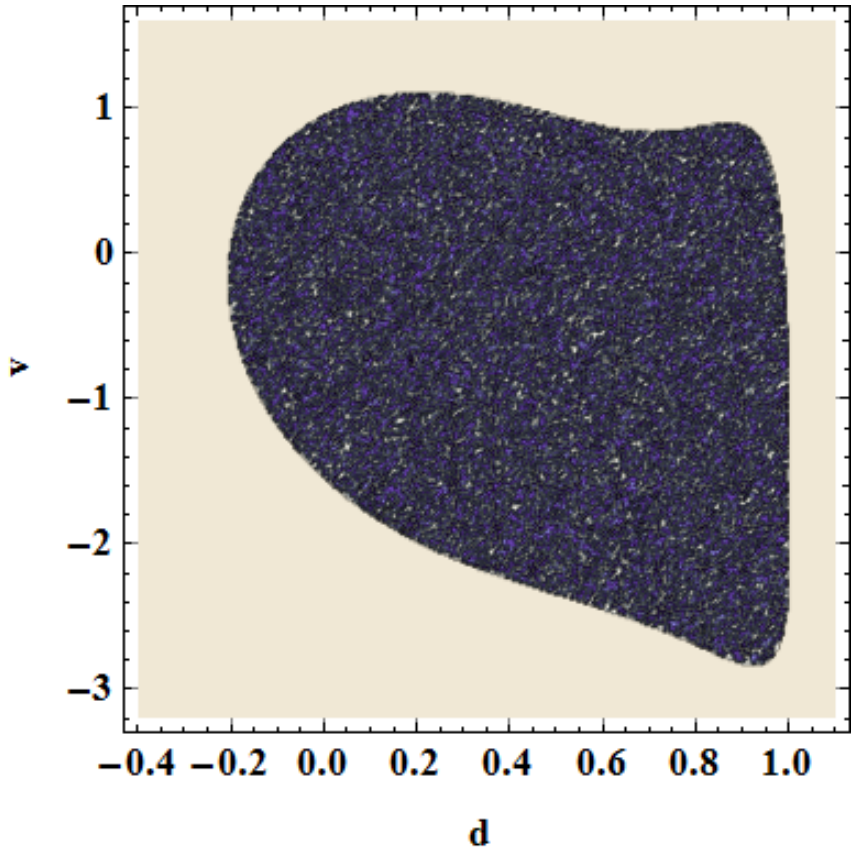

Figure 4.27: Basin of attraction of chaotic attractor at $\omega = 1.2$ and $V_{AC} = 3.5V$.

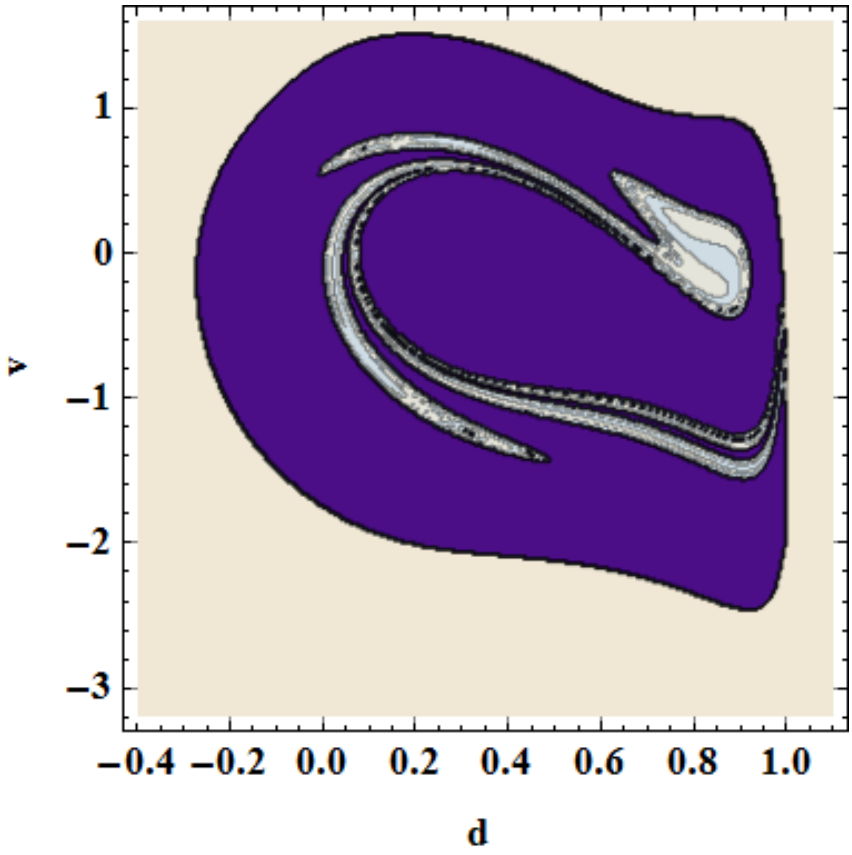

Figure 4.28: Basin of attraction at $\omega = 7.5$ and $V_{AC} = 2V$.

environments with noise to add more robustness to the sensor.

4.5 Experimental Issues

For the families of beams used in experiments, a nondimensional natural frequency of $\omega = 2$ is equivalent a frequency of 60-100 kHz. Working in this frequency range requires special Op-Amps with high GBP. These Op-Amps are more vulnerable to instabilities. The parasitic capacitances existing due to the bread-board when combined with environment noise are sufficient to convert each Op-Amp into a self-excited oscillator. In order to overcome this, a Printed Circuit Board (PCB) is used to implement the controller of the chaotic resonator.

Figure 4.29 shows the controller implemented on a PCB. Potentiometers are used to give flexibility in changing the values of the voltage gain G, the displacement gain Ψ, the integrator gain (to account for different vibrometer dynamic ranges), and the beam time constant T.

In testing the controller, we could not relate the input to the output of the controller. Troubleshooting was not possible on the PCB since it was not equipped with intermediate test points. Another PCB should be designed with test points and jumpers in order to be able to test and troubleshoot each stage separately .

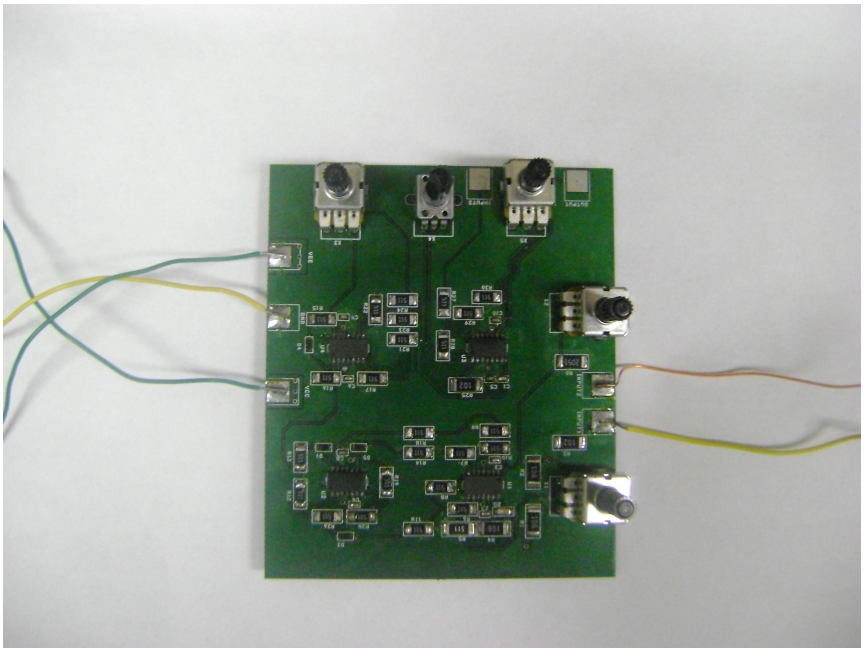

Figure 4.29: Chaotic actuator controller implemented on a PCB.

Chapter 5

Conclusion and Future Work

An analog electronic controller has been realized for an electrostatically actuated micro-cantilever beam. Using the controller, the close-loop system can be utilized as a robust actuator and a mass sensor. The controller gains can be adjusted so that the system is uni-stable or bi-stable. For the uni-stable system, the pull-in instability is removed and simulations show the controller's ability to position the beam tip to over 90% of the gap in smooth stable operation. The controller has been realized on a bread-board and tested successfully. Preliminary testing of the close-loop system showed stable motions beyond the pull-in limit as well as good matching with the model.

When the controller is adjusted to have bi-stability, chaotic regions appear and the system can be utilized as a sensor. Dynamic analysis of the close-loop system has been conducted. Period-doubling bifurcations, chaos, transient chaos, and super-harmonic orbits have been observed and analyzed. By generating four bifurcation diagrams for different actuation voltages, the dynamic behavior of the system at any region can now be determined. The best operating regions for the chaotic actuation have been identified and proven to be suitable for use as a sensing mechanism. The high frequency version of the controller has been designed and realized on a PCB.

For the actuator, the next step will be pursuing a stable travel up to 90% of the gap experimentally. After that, design and fabrication of a complete on chip system is to be pursued. A piezo-electric material will be used as a position sensor instead of the vibrometer, and in this case there will be no need for an integrator in the controller circuit. But on the other hand, the sensor dynamics must be put in account and compensated for.

As for the sensor, the same steps as for the actuator are needed in addition to identifying a robust routine for relating changes in the chaotic behavior with changes in the system parameters.

Bibliography

[1] S. Towfighian, A. Seleim, E. M. Abdel-Rahman, and G. R. Heppler, "Experimental validation for an extended-stability electrostatic actuator," in *ASME IDETC Conference*, no. DETC2010-28983, (Montreal Quebec, Canada), August 2010 2010. x, 13, 40

[2] *Vibrometer Controller OFV-5000 (User Manual).* x, 14, 15

[3] S. Kamisuki, T. Hagata, C. Tezuka, Y. Nose, M. Fujii, and M. Atobe, "A low power, small, electrostatically-driven commercial inkjet head," in *Microelectromechanical Systems, 1998. MEMS 98. Proceedings., The Eleventh Annual International Workshop on*, pp. 63–68, 1998. 1

[4] F. G. Tseng, C. J. Kim, and C. M. Ho, "A high-resolution high-frequency monolithic top-shooting microinjector free of satellite drops-part I: concept, design, and model," *Journal of Microelectromechanical Systems*, vol. 11, no. 5, pp. 427–436, 2002. 1

[5] S. S. Baek, H. T. Lim, H. Song, Y. S. Kim, K. D. Bae, C. Cho, C. S. Lee, J. W. Shin, S. J. Shin, K. Kuk, *et al.*, "A novel back-shooting inkjet printhead using trench-filling and SOI wafer," *Sensors & Actuators: A. Physical*, vol. 114, no. 2-3, pp. 392–397, 2004. 1

[6] A. K. Sen and J. Darabi, "Droplet ejection performance of a monolithic thermal inkjet print head," *Journal of Micromechanics and Microengineering*, vol. 17, pp. 1420–1427, 2007. 1

[7] N. T. Nguyen, X. Huang, and T. K. Chuan, "MEMS-micropumps: a review.," *Journal of Fluids Engineering(Transactions of the ASME)*, vol. 124, no. 2, pp. 384–392, 2002. 1

[8] G. M. Rebeiz, *RF MEMS: theory, design, and technology.* John Wiley and Sons, 2003. 1

[9] J. J. Yao, "Topical review," *Journal of micromechanics and microengineering*, vol. 10, pp. R9–R38, 2000. 1

[10] H. Xie, Y. Pan, and G. K. Fedder, "Endoscopic optical coherence tomographic imaging with a CMOS-MEMS micromirror," *Sensors & Actuators: A. Physical*, vol. 103, no. 1-2, pp. 237–241, 2003. 1

[11] P. H. Tran, D. S. Mukai, M. Brenner, and Z. Chen, "In vivo endoscopic optical coherence tomography by use of a rotational microelectromechanical system probe," *Optics letters*, vol. 29, no. 11, pp. 1236–1238, 2004. 1

[12] J. M. Zara and S. W. Smith, "A micromachine high frequency ultrasound scanner using photolithographic fabrication," *IEEE transactions on ultrasonics, ferroelectrics, and frequency control*, vol. 49, no. 7, pp. 947–958, 2002. 1

[13] K. J. Rebello, "Applications of MEMS in surgery," *Proceedings of the IEEE*, vol. 92, no. 1, pp. 43–55, 2004. 1

[14] D. H. Kim, B. Kim, and H. Kang, "Development of a piezoelectric polymer-based sensorized microgripper for microassembly and micromanipulation," *Microsystem technologies*, vol. 10, no. 4, pp. 275–280, 2004. 1

[15] T. Tanikawa, T. Arai, and T. Masuda, "Development of micro manipulation system with two-finger micro hand," vol. 2, 1996. 1

[16] J. W. L. Zhou, H. Y. Chan, T. K. H. To, K. W. C. Lai, and W. J. Li, "Polymer MEMS actuators for underwater micromanipulation," *IEEE/ASME Transactions on Mechatronics*, vol. 9, no. 2, pp. 334–342, 2004. 1

[17] M. C. Carrozza, A. Eisinberg, A. Menciassi, D. Campolo, S. Micera, and P. Dario, "Force-controlled microgripper," *Journal of Micromechanics and Microengineering*, vol. 10, pp. 271–276, 2000. 1

[18] B. Solano and D. Wood, "Design and testing of a polymeric microgripper for cell manipulation," *Microelectronic Engineering*, vol. 84, no. 5-8, pp. 1219–1222, 2007. 1

[19] K. Kim, X. Liu, Y. Zhang, and Y. Sun, "Nanonewton force-controlled manipulation of biological cells," *Journal of Micromechanics and Microengineering*, vol. 18, pp. 1–8, 2008. 1

[20] L. R. Carley, J. A. Bain, G. K. Fedder, D. W. Greve, D. F. Guillou, M. S. C. Lu, T. Mukherjee, S. Santhanam, L. Abelmann, and S. Min, "Single-chip computers with microelectromechanical systems-based magnetic memory (invited)," *Journal of Applied Physics*, vol. 87, pp. 6680–6685, 2000. 1

[21] D. J. Bell, T. J. Lu, N. A. Fleck, and S. M. Spearing, "MEMS actuators and sensors: observations on their performance and selection for purpose," *Journal of Micromechanics and Microengineering*, vol. 15, pp. S153–S164, 2005. 1

[22] E. S. Hung and S. D. Senturia, "Extending the travel range of analog-tuned electrostatic actuators," *Microelectromechanical Systems, Journal of*, vol. 8, no. 4, pp. 497–505, 1999. 1, 4

[23] S. D. Senturia, *Microsystem design*. Kluwer Academic Publishers, 2001. 2, 9

[24] A. H. Nayfeh, M. I. Younis, and E. M. Abdel-Rahman, "Dynamic pull-in phenomenon in MEMS resonators," *Nonlinear Dynamics*, vol. 48, no. 1, pp. 153–163, 2007. 3

[25] H. P. Lang, R. Berger, F. Battiston, J. P. Ramseyer, E. Meyer, C. Andreoli, J. Brugger, P. Vettiger, M. Despont, T. Mezzacasa, *et al.*, "A chemical sensor based on a micromechanical cantilever array for the identification of gases and vapors," *Applied Physics A: Materials Science & Processing*, vol. 66, pp. 61–64, 1998. 3

[26] W. Zhang, R. Baskaran, and K. L. Turner, "Effect of cubic nonlinearity on auto-parametrically amplified resonant MEMS mass sensor," *Sensors & Actuators: A. Physical*, vol. 102, no. 1-2, pp. 139–150, 2002. 3

[27] C. Ziegler, "Cantilever-based biosensors," *Analytical and bioanalytical chemistry*, vol. 379, no. 7, pp. 946–959, 2004. 3

[28] T. Bachels and R. Schafer, "Microfabricated cantilever-based detector for molecular beam experiments," *Review of Scientific Instruments*, vol. 69, pp. 3794–3797, 1998. 3

[29] S. Cherian, R. K. Gupta, B. C. Mullin, and T. Thundat, "Detection of heavy metal ions using protein-functionalized microcantilever sensors," *Biosensors and Bioelectronics*, vol. 19, no. 5, pp. 411–416, 2003. 3

[30] E. A. Wachter and T. Thundat, "Micromechanical sensors for chemical and physical measurements," *Review of Scientific Instruments*, vol. 66, p. 3662, 1995. 3

[31] M. Khater, E. Abdel-Rahman, and A. Nayfeh, "A mass sensing technique for electrostatically-actuated mems," in *International Design Engineering Technical Conferences & Computers and Information in Engineering Conference, ASME 2009*, 2009. 3

[32] R. Legtenberg, J. Gilbert, S. D. Senturia, and M. Elwenspoek, "Electrostatic curved electrode actuators," *Journal of Microelectromechanical Systems*, vol. 6, no. 3, pp. 257–265, 1997. 4

[33] J. I. Seeger and S. B. Crary, "Stabilization of electrostatically actuated mechanical devices," vol. 2, 1997. 4

[34] E. K. Chan and R. W. Dutton, "Electrostatic micromechanical actuator with extended range of travel," *Journal of microelectromechanical Systems*, vol. 9, no. 3, pp. 321–328, 2000. 4

[35] J. I. Seeger and B. E. Boser, "Dynamics and control of parallel-plate actuators beyond the electrostatic instability," in *Transducers*, vol. 99, pp. 474–477, Citeseer, 1999. 4

[36] J. I. Seeger and B. E. Boser, "Charge control of parallel-plate, electrostatic actuators and the tip-in instability," *Journal of Microelectromechanical Systems*, vol. 12, no. 5, pp. 656–671, 2003. 4

[37] P. B. Chu and S. J. Pister, "Analysis of closed-loop control of parallel-plate electrostatic microgrippers," in *1994 IEEE International Conference on Robotics and Automation, 1994. Proceedings.*, pp. 820–825, 1994. 4

[38] M. S. C. Lu and G. K. Fedder, "Position control of parallel-plate microactuators for probe-based data storage," *Journal of Microelectromechanical Systems*, vol. 13, no. 5, pp. 759–769, 2004. 5, 12

[39] L. A. Rocha, E. Cretu, and R. F. Wolffenbuttel, "Using dynamic voltage drive in a parallel-plate electrostatic actuator for full-gap travel range and positioning," *Journal of Microelectromechanical Systems*, vol. 15, no. 1, p. 69, 2006. 5

[40] S. Liu, A. Davidson, and Q. Lin, "Simulation studies on nonlinear dynamics and chaos in a MEMS cantilever control system," *Journal of Micromechanics and Microengineering*, vol. 14, no. 7, pp. 1064–1073, 2004. 5

[41] S. Towfighian, G. R. Heppler, and E. M. Abdel-Rahman, "Analysis of a chaotic electrostatic micro-oscillator," *Journal of Computational and Nonlinear Dynamics*, in press. 5, 16, 42

[42] S. H. Strogatz, *Nonlinear dynamics and chaos: With applications to physics, biology, chemistry, and engineering*. Perseus Books, 2001. 5

[43] A. H. Nayfeh and B. Balachandran, *Applied nonlinear dynamics*. Wiley New York, 1995. 5, 46, 48, 60

[44] S. H. Ghafari, F. Golnaraghi, and F. Ismail, "Effect of localized faults on chaotic vibration of rolling element bearings," *Nonlinear Dynamics*, vol. 53, no. 4, pp. 287–301, 2008. 5

[45] S. H. Yin and B. I. Epureanu, "Experimental Enhanced Nonlinear Dynamics and Identification of Attractor Morphing Modes for Damage Detection," *Journal of Vibration and Acoustics*, vol. 129, p. 763, 2007. 5

[46] B. I. Epureanu, S. H. Yin, and E. H. Dowell, "Enhanced nonlinear dynamics for accurate identification of stiffness loss in a thermo-shielding panel," *Nonlinear Dynamics*, vol. 39, no. 1, pp. 197–211, 2005. 6

[47] Y. T. Wu, K. K. Shyu, T. R. Chen, and W. Y. Guo, "Using three-dimensional fractal dimension to analyze the complexity of fetal cortical surface from magnetic resonance images," *Nonlinear Dynamics*, pp. 1–8, 2009. 6

[48] J. Bienstman, J. Vandewalle, and R. Puers, "The autonomous impact resonator: a new operating principle for a silicon resonant strain gauge," *Sensors & Actuators: A. Physical*, vol. 66, no. 1-3, pp. 40–49, 1998. 6

[49] Y. C. Wang, S. G. Adams, J. S. Thorp, N. C. MacDonald, P. Hartwell, and F. Bertsch, "Chaos in MEMS, parameter estimation and its potential application," *IEEE Transactions on Circuits and Systems I: Fundamental Theory and Applications*, vol. 45, no. 10, pp. 1013–1020, 1998. 6

[50] B. E. DeMartini, H. E. Butterfield, J. Moehlis, and K. L. Turner, "Chaos for a microelectromechanical oscillator governed by the nonlinear Mathieu equation," *Journal of Microelectromechanical Systems*, vol. 16, no. 6, pp. 1314–1323, 2007. 6

[51] S. K. De and N. R. Aluru, "Complex oscillations and chaos in electrostatic microelectromechanical systems under superharmonic excitations," *Physical review letters*, vol. 94, no. 20, p. 204101, 2005. 6

[52] F. Najar, A. H. Nayfeh, E. M. Abdel-Rahman, S. Choura, and S. El-Borgi, "Dynamics and Global Stability of Beam-based Electrostatic Microactuators," *Journal of Vibration and Control*, 2010. 6

[53] M. Malek-Zavarei and M. Jamshidi, *Time-delay systems: analysis, optimization and applications*. Elsevier Science Inc. New York, NY, USA, 1987. 13

[54] *VD-02 Velocity Decoder*. 15

[55] A. S. Sedra and K. C. Smith, *Microelectronic circuits*. Oxford University Press, USA, 1997. 18, 20, 21, 22, 24, 27

[56] S. Towfighian, *Mass Sensing Using Chaotic Micro-oscillators*. PhD thesis, University of Waterloo, Under preparation. 32, 68

[57] B. Carnahan, H. A. Luther, and J. O. Wilkes, *Applied numerical methods*. Wiley New York, 1969. 45

[58] R. H. Simoyi, A. Wolf, and H. L. Swinney, "One-dimensional dynamics in a multi-component chemical reaction," *Physical Review Letters*, vol. 49, no. 4, pp. 245–248, 1982. 60